AĞRI İBRAHİM ÇEÇEN UNIVERSITY 2007

EASTERN ANATOLIAN JOURNAL OF SCIENCE 2015

PREFACE

Dear scientist,

I am happy to announce that Volume VIII - Issue II of the Eastern Anatolian Journal of Science (EAJS) has been published. This issue is composed of 4 research articles that possess some of the leading and advanced techniques of natural and applied sciences. On behalf of the owner of EAJS, I would like to thank all authors, referees, our editorial board members and section editors that provide valuable contributions for the publication of the issue.

EAJS will publish original and high-quality articles covering a wide range of topics in scientific research, dedicated to promoting high standards and excellence in the creation and dissemination of scientific knowledge. EAJS published in English is open access journal and abstracting and indexing by various international index services.

Authors are solicited to contribute to the EAJS by submitting articles that illustrate research results, projects, surveying works and industrial experiences that describe significant advances in the following areas, but are not limited to:

- ➢ Biology
- ➢ Chemistry
- ➢ Engineering
- ➢ Mathematics
- ➢ Nanoscience and Nanotechnology
- ➢ Physics

Our previous issues have an attraction in terms of scientific quality and impact factor of articles by favorable feedbacks of readers. Our editorial team lend wings to be an internationally reputable and pioneer journal of science by their outstanding scientific personality. I am hoping to work effectively with our editorial team in the future.

I'd like to express my gratitude to all authors, members of editorial board and contributing reviewers. My sincere thanks go to Prof. Dr. Abdulhalik KARABULUT, the rector of Ağrı İbrahim Çeçen University, sets the goal of being also a top-ranking university in scientific sense, for supporting and motivating us in every respect. I express my gratitude to the members of technical staff of the journal for the design and proofreading of the articles. Last but not least, my special thanks go to the respectable businessman Mr. İbrahim ÇEÇEN who unsparingly supports our university financially and emotionally, to his team and to the director and staff of IC foundation.

I invite scientists from all branches of science to contribute our journal by sending papers for publication in EAJS.

Prof. Dr. İbrahim HAN

Editor-in-Chief

CONTENTS

Coefficient Bound Estimates and Fekete-Szegö Problem
for a Certain Class of Analytic Functions

Nizami MUSTAFA[1*] and Semra KORKMAZ[2]

[1] Kafkas University, Faculty of Science and Letters, Department of Mathematics, Kars, Turkey,
nizammstafa@gmail.com (ORCID:0000-0002-2758-0274)
[2] Kafkas University, Faculty of Science and Letters, Department of Mathematics, Kars, Turkey,
korkmazsemra36@outlook.cm

Abstract

In this study, we introduce and examine a certain subclass of analytic functions on the open unit disk in the complex plane. Here, we give coefficient bound estimates and investigate the Fekete-Szegö problem for this class. Some interesting special cases of the results obtained here are also discussed.

1. Introduction

Let $U = \{z \in \mathbb{C}: |z| < 1\}$ and $H(U)$ denote the class of analytic functions in U. By A we denote the class of all functions $f \in H(U)$ given by

$$f(z) = z + a_2 z^2 + \cdots + a_n z^n + \cdots$$
$$= z + \sum_{n=2}^{\infty} a_n z^n , z \in \mathbb{C}$$
(1)

Let S denote the class of all univalent functions in A. For $\alpha \in [0,1)$, some of the important and well-investigated subclasses of S include the classes

$S^*(\alpha)$ and $C(\alpha)$, respectively, starlike and convex function classes of order α in U. By definition, we have

$$S^*(\alpha) = \left\{ f \in S : \text{Re}\, \frac{zf'(z)}{f(z)} > \alpha,\ z \in U \right\} \text{ and}$$

$$C(\alpha) = \left\{ f \in S : \text{Re}\left(1 + \frac{zf''(z)}{f'(z)} \right) > \alpha,\ z \in U \right\}.$$

For the functions f and g which are analytic in U, f is said to be subordinate to g and denoted as $f(z) \prec g(z)$ if there exists an analytic function ω such that

$$\omega(0) = 0,\ |\omega(z)| < 1 \text{ and } f(z) = g(\omega(z)).$$

As it is known that the coefficient problem is one of the important subjects of the theory of geometric functions. Many researchers have introduced and investigated several interesting subclasses of analytic functions and they have found some estimates on the first two coefficients of the functions belonging to these subclasses (see Brannan, D.A. and Clunie, J. 1980, Brannan, D.A. and Taha, T.S. 1986, Lewin, M. 1967, Netanyahu, E. 1969, Srivastava, H.M., Mishra, A.K. and Gochhayat, P. 2010, Xu, Q.H., Xiao, G. and Srivastava, H.M. 2012).

The functional $H_2(1) = a_3 - a_2^2$ is known as the Fekete-Szegö functional and one usually considers the further generalized functional $H_2(1) = a_3 - \mu a_2^2$, where μ is a complex or real number (see Fekete, M.

and Szegö, G. 1993), and is an important tool in the theory of analytic functions. Estimating the upper bound of $\left|a_3 - \mu a_2^2\right|$ is known as the Fekete-Szegö problem in the theory of analytic functions. The Fekete-Szegö problem has been investigated by many mathematicians for several subclasses of analytic functions (see Mustafa, N. 2017, Mustafa, N. and Gündüz, M.C. 2019, Zaprawa, P. 2014). Very recently, Mustafa and Mrugusundaramoorthy (Mustafa, N. and Murugusundaramoorthy, G. 2021) introduced a subclass of bi-univalent functions related to shell shaped region and they examined the Fekete-Szegö problem for this subclass.

Now, let we define the following subclass of analytic and univalent functions.

Definition 1.1. A function $f \in S$ is said to be in the class $S^*(\varphi)$ if the following condition is satisfied

$$\frac{zf'(z)}{f(z)} \prec \varphi(z), \ z \in U.$$

In this definition, $\varphi(z) = z + \sqrt{1+z^2}$ and the branch of the square root is chosen with the initial value $\varphi(0) = 1$. It can be easily seen that the function $\varphi(z) = z + \sqrt{1+z^2}$ maps the unit disc U onto a shell shaped region on the right half plane and it is analytic and univalent in U. The range $\varphi(U)$ is symmetric respect to real axis and φ is a function with positive real part in U with $\varphi(0) = \varphi'(0) = 1$. Moreover, it is a starlike domain with respect to point $\varphi(0) = 1$.

Let, P be the set of the functions $p(z)$ analytic in U and satisfying $\operatorname{Re}(p(z)) > 0, \ z \in U$ and $p(0) = 1$, with power series

$$p(z) = 1 + p_1 z + p_2 z^2 + p_3 z^3 + \cdots + p_n z^n + \cdots$$
$$= 1 + \sum_{n=1}^{\infty} p_n z^n, \ z \in U.$$

In order to prove our main results, we shall need the following lemmas concerning functions with positive real part (see Duren, P.L. 1983, Grenander, U. and Szegö, G. 1958).

Lemma 1.2. Let $p \in P$, then $|p_n| \leq 2, \ n = 1, 2, 3, \ldots$ and

$$\left|p_2 - \frac{c}{2} p_1^2\right| \leq 2 \cdot \max\{1, |c-1|\}$$

$$= 2 \cdot \begin{cases} 1 & if \ c \in [0, 2], \\ |c-1| & elsewhere. \end{cases}$$

Lemma 1.3. Let $p \in P$, then $|p_n| \leq 2$ for every $n = 1, 2, 3, \ldots$ and

$$2p_2 = p_1^2 + \left(4 - p_1^2\right)x,$$

$$4p_3 = p_1^3 + 2\left(4 - p_1^2\right)p_1 x - 2\left(4 - p_1^2\right)p_1 x^2$$
$$+ 2\left(4 - p_1^2\right)\left(1 - |x|^2\right)z$$

for some x and z with $|x| < 1$ and $|z| < 1$.

Lemma 1.4. Let $p \in P$, $B \in [0, 1]$ and $B(2B-1) \leq D \leq B$, then

$$\left|p_3 - 2Bp_1 p_2 + Dp_1^3\right| \leq 2.$$

Remark 1.5. As it can be seen from the serial expansion of the function φ given in Definition 1.1, this function belongs to the class P.

In this paper, we give an upper bound estimate for the coefficients of the functions belonging to the class $S^*(\varphi)$ and examine the Fekete-Szegö problem for this class.

2. Main results

In this section, firstly we give the following theorem on the coefficient bound estimates for the class $S^*(\varphi)$.

Theorem 2.1. Let the function $f \in H(U)$ given by (1) be in the class $S^*(\varphi)$. Then,

$$|a_2| \leq 1, \ |a_3| \leq \frac{3}{4} \text{ and } |a_4| \leq \frac{5}{6}.$$

Proof. Let the function $f \in H(U)$ given by (1) be in the class $S^*(\varphi)$. Then, according to Definition 1.1 there is an analytic function $\omega : U \to U$ with $\omega(0) = 0$ and $|\omega(z)| < 1$ satisfying the following condition

$$\frac{zf'(z)}{f(z)} = \varphi(\omega(z)) = \omega(z) + \sqrt{1 + \omega^2(z)}, \ z \in U.$$
$$(2)$$

Now, let us define the function $p \in P$ as follows

$$p(z) = \frac{1 + \omega(z)}{1 - \omega(z)} = 1 + p_1 z + p_2 z^2 + p_3 z^3 + \cdots$$

$$= 1 + \sum_{n=1}^{\infty} p_n z^n, \ z \in U.$$

From here, we get the following expression for the function ω

$$\omega(z) = \frac{p(z) - 1}{p(z) + 1}$$

$$= \frac{1}{2} \left[\begin{array}{c} p_1 z + \left(p_2 - \frac{p_1^2}{2} \right) z^2 \\ + \left(p_3 - p_1 p_2 + \frac{p_1^2}{4} \right) z^3 + \cdots \end{array} \right], z \in U.$$
$$(3)$$

If we use series expansion of the function $\sqrt{1 + \omega^2(z)}$ and change the expression of the function ω in (2) with the expression in (3), from (2), we obtain

$$\frac{zf'(z)}{f(z)} = 1 + \frac{p_1}{2} z + \left(\frac{p_2}{2} - \frac{p_1^2}{8} \right) z^2$$

$$+ \left(\frac{p_3}{2} - \frac{p_1 p_2}{4} \right) z^3 + \cdots, \ z \in U.$$
$$(4)$$

If we make the necessary operations and simplifications in Equation (4) and the coefficients of the same order terms on the left and right sides of the equality are equalized, then the following expressions are obtained for the coefficients a_2, a_3 and a_4

$$2a_2 = p_1, \ 2a_3 - a_2^2 = \frac{p_2}{2} - \frac{p_1^2}{8},$$

$$3a_4 - 3a_2 a_3 + a_2^3 = \frac{p_3}{2} - \frac{p_1 p_2}{4}.$$

From these equalities, we can write

$$a_2 = \frac{p_1}{2}, \tag{5}$$

$$a_3 = \frac{1}{2} a_2^2 + \frac{1}{4} \left(p_2 - \frac{p_1^2}{4} \right), \tag{6}$$

$$a_4 = a_2 a_3 - \frac{1}{3} a_2^3 + \frac{1}{6} \left(p_3 - \frac{p_1 p_2}{2} \right). \tag{7}$$

By applying Lemma 1.2 to the equality (5), we immediately obtain the first result of the theorem. Now firstly, considering (5), then using the Lemma 1.3 and applying the triangle inequality to the equality (6), we get the following inequality for $|a_3|$

$$|a_3| \leq \frac{3}{16} t^2 + \frac{4 - t^2}{8} \xi, \ \xi \in (0,1)$$

with $\xi = |x| < 1$. By maximizing the right-hand side of this inequality with respect to parameter ξ, we obtain

$$|a_3| \leq \frac{3}{16} t^2 + \frac{4 - t^2}{8}, \ t \in [0,2].$$

Therefore,

$$|a_3| \leq \frac{t^2}{16} + \frac{1}{2}, \ t \in [0,2].$$

From the last inequality, we obtain the second result of the theorem.

Now let's find an upper bound estimate for the coefficient a_4. From equalities (5) - (7), we get

$$a_4 = \frac{p_1}{8}\left(p_2 - \frac{p_1^2}{4}\right) + \frac{1}{6}\left(p_3 - \frac{p_1 p_2}{2} + \frac{p_1^3}{8}\right);$$

that is,

$$a_4 = \frac{p_1}{8}\left(p_2 - \frac{c}{2}p_1^2\right) + \frac{1}{6}\left(p_3 - 2Bp_1p_2 + Dp_1^3\right),$$

with $c = \frac{1}{2}$, $B = \frac{1}{4}$ and $D = \frac{1}{8}$.

Applying the triangle inequality to the last equality, we obtain

$$|a_4| \leq \frac{|p_1|}{8}\left|p_2 - \frac{c}{2}p_1^2\right| + \frac{1}{6}\left|p_3 - 2Bp_1p_2 + Dp_1^3\right|.$$

From this, applying Lemma 1.2 and Lemma 1.4, we obtain the desired upper bound estimate for $|a_4|$. With this, the proof of Theorem 2.1 is completed.

Now, we give the following theorem on the Fekete-Szegö problem for the class $S^*(\varphi)$.

Theorem 2.2. Let the function $f \in H(U)$ given by (1) be in the class $S^*(\varphi)$ and $\mu \in \mathbb{C}$. Then,

$$|a_3 - \mu a_2^2| \leq \frac{1}{4} \cdot \begin{cases} 2 & if \ 2|1-2\mu| \leq 1, \\ 2|1-2\mu|+1 & if \ 2|1-2\mu|>1. \end{cases}$$

Proof. Let the function $f \in H(U)$ given by (1) be in the class $S^*(\varphi)$ and $\mu \in \mathbb{C}$. Then, from the expressions of the coefficients a_2 and a_3, obtained in the equalities (5) and (6), we write the following expression for $a_3 - \mu a_2^2$

$$a_3 - \mu a_2^2 = \frac{1}{2}(1-2\mu)a_2^2 + \frac{1}{4}\left(p_2 - \frac{p_1^2}{4}\right).$$

Considering (5) and using Lemma 1.3, the above expression can be written as follows

$$a_3 - \mu a_2^2 = \frac{1}{8}\left[(1-2\mu)p_1^2 + \frac{p_1^2}{2} + \left(4 - p_1^2\right)x\right]$$

for some x with $|x| < 1$. From this, using the triangle inequality we obtain

$$|a_3 - \mu a_2^2| \leq \frac{1}{8}\left\{\left[|1-2\mu| + \frac{1}{2}\right]t^2 + \left(4 - t^2\right)\xi\right\},$$

$$\xi \in (0,1),$$

with $\xi = |x|$. If we maximize the right-hand side of this inequality with respect to the parameter ξ, we get

$$|a_3 - \mu a_2^2| \leq \frac{1}{8}\left\{\left[|1-2\mu| - \frac{1}{2}\right]t^2 + 4\right\}, \ t \in [0,2]$$

.

Then, by maximizing the right-hand side of the last inequality with respect to the variable t, we arrive at the result of the theorem.

Thus, the proof of the Theorem 2.2 is completed.

3. Conclusions

In this section, we will focus on some special and general cases of the obtained results in the previous section.

In the case of $\mu \in \mathbb{R}$ the following theorem is easily proved.

Theorem 3.1. Let the function $f \in H(U)$ given by (1) be in the class $S^*(\varphi)$ and $\mu \in \mathbb{R}$. Then,

$$|a_3 - \mu a_2^2| \leq \frac{1}{4} \cdot \begin{cases} 2 & if \ \frac{1}{4} \leq \mu \leq \frac{3}{4}, \\ 2|1-2\mu|+1 & if \ \mu < \frac{1}{4} \ or \ \mu > \frac{3}{4}. \end{cases}$$

If we take $\mu = 0$ and $\mu = 1$ respectively in Theorem 3.1, we get the following results.

Corollary 3.2. Let $f \in S^*(\varphi)$, then $|a_3| \leq \frac{3}{4}$.

Corollary 3.3. Let $f \in S^*(\varphi)$, then

$$|a_3 - a_2^2| \leq \frac{3}{4}.$$

NOTE: We would like to point out that we can also find the results obtained in the study for the class

$$M(\varphi, \beta) = \left\{ \begin{array}{l} f \in S : \ (1-\beta)\dfrac{zf'(z)}{f(z)} \\ +\beta\dfrac{zf''(z)}{f'(z)} \prec \varphi(z), z \in U \end{array} \right\},$$

$\beta \in [0,1].$

It is clear that the $M(\varphi, \beta)$-class is more general version of the class $S^*(\varphi)$. In fact, it is clear that

$$S^*(\varphi) = M(\varphi, 1).$$

References

BRANNAN, D.A. & CLUNIE, J. (1980). Aspects of contemporary complex analysis. Academic Press, London and New York, USA.

BRANNAN, D.A. & TAHA, T.S. (1986). On some classes of bi-univalent functions. Studia Univ. *Babes-Bolyai Mathematics,* 31, 70-77.

DUREN, P.L. (1983). Univalent Functions. In: Grundlehren der Mathematischen Wissenschaften, Band 259, New- York, Berlin, Heidelberg and Tokyo, Springer-Verlag.

GRENANDER, U. & SZEGÖ, G. (1958). Toeplitz Form and Their Applications. California Monographs in Mathematical Sciences, University California Press, Berkeley.

FEKETE, M. & SZEGÖ, G. (1993). Eine Bemerkung Über Ungerade Schlichte Funktionen. *Journal of the London Mathematical Society,* 8, 85-89.

LEWIN, M. (1967). On a coefficient problem for bi-univalent functions. Proceedings of the American Mathematical Society, 18, 63-68.

MUSTAFA, N. (2017). Fekete-Szegö Problem for Certain Subclass of Analytic and Bi-Univalent Functions. *Journal of Scientific and Engineering Reserch*, 4(8), 30-400.

MUSTAFA, N. & GÜNDÜZ, M.C. (2019). The Fekete-Szegö Problem for Certain Class of Analytic and Univalent Functions. *Journal of Scientific and Engineering Reserch,* 6(5), 232-239.

MUSTAFA,N. & MURUGUSUNDARAMOORTHY, G. (2021). Second Hankel Determinant for Mocanu Type Bi-Starlike Functions Related to Shell Shaped Region. *Turkish Journal of Mathematics,* 45, 1270-1286.

NETANYAHU, E. (1969). The minimal distance of the image boundary from the origin and the second coefficient of a univalent function. *Archive for Rational Mechanics and Analysis,* 32, 100-112.

SRIVASTAVA, H.M., MISHRA, A.K. and GOCHHAYAT, P. (2010). Certain subclasses of analytic and bi-univalent functions. *Applied Mathematics Letters,* 23, 1188-1192.

ZAPRAWA, P. (2014). On the Fekete- Szegö Problem for the Classes of Bi-Univalent Functions. *Bulletin of the Belgain Mathematical Society,* 21, 169-178.

XU, Q.H., XIAO, G. and SRIVASTAVA, H.M. (2012). A certain general subclass of analytic and bi-univalent functions and associated coefficient estimate problems. Applied Mathematics and Computation, 218, 11461-11465.

A Combined 3D-QSAR, Pharmacophore Modelling, and Molecular Docking Study for Plastoquinone Analogues

Mehmet ÇINAR[1*]

[1] *Bayburt University, Vocational School of Technical Sciences, Electricity and Energy Department, Bayburt, Turkey*
cnr.mehmet@gmail.com (ORCID:0000-0002-0184-0082)

Abstract

In this study, a set consisting of 39 compounds that are in the literature and carrying Plastoquinone analogues was investigated. The 3D-QSAR study was performed using a field-based method and Partial Least Square (PLS) regression analysis. The generated 3D-QSAR model has sufficient statistical significance and acceptable prediction power with the regression correlation coefficient (r^2) at 0.97 and $q^2 = 0.4$. The pharmacophore modelling was carried out and a four-point model (AHHR_3) was generated. Molecular docking was performed with the selected 1IEP protein and the RMSD value for the position of the ligands docked at the two identified active sites was obtained as 0.3669 Å and 0.5535 Å. Docking analysis revealed that the ABQ16 is the best docked ligand with a DockScore of -9.55, followed by AQ2, AQ6 and ABQ11 with scores of -8.56, -8.2 and -7.64, respectively. It was seen that hydrophobic interactions are dominate and the TYR253 residue is responsible for the pi-pi interaction with the aromatic ring.

Keywords: Plastoquinone Analogues, 3D-QSAR, Pharmacophore Modelling, Molecular Docking, Charge Density

1. Introduction

Cancer is one of the major public health problems that affects people all over the world regardless of sex, age, race or socioeconomic status. According to the World Health Organization (WHO), "Cancer arises from the transformation of normal cells into tumour cells in a multi-stage process that generally progresses from a pre-cancerous lesion to a malignant tumour." It is the second leading cause of death globally, and causes approximately 10 million deaths per year. It was estimated that more than 1.800.000 cancer cases of different types will be diagnosed in the USA and will cause more than 600.000 deaths in total for the 2020 (Siegel et al., 2016). For this reason, various treatment methods -including surgery- and drugs have been developed to struggle this fatal disease, which has many different types. Chemotherapy is one of the most common treatments used to slowdown the growth of cancer cells or kill cancer cells (Brannon-Peppas & Blanchette, 2004), but chemotherapeutic resistance appears to occur in cancer cells over time, as well as many negative side effects of chemotherapy (Wellington, 2015). Moreover, each cancer type expresses a different drug-resistant gene sequence, and cancerous cells show enormous heterogeneity with respect to drug resistance. The rapid growth of drug-resistant variants because of strong selection imposed by anti-cancer drugs causes many cancers to rapidly acquire drug resistance (Gottesman, 2001). In addition, more than 95% of drugs/compounds that kill cancer cells in culture or regress tumors in studies for animals fail in Phase I studies for humans. Although approved by regulatory agencies such as the FDA, many anticancer drugs have been shown to have no effect on the survival of cancer patients or can provide an increase in overall survival in few months

(Kunnumakkara et al., 2019). Since more than one genos causes many types of cancer, multi-targeted therapies are needed for cancer prevention and treatment, and new anticancer drugs continue to be developed. In addition to advanced clinical trials, products in the drug discovery market are also being improved with new and advanced technologies. Several approaches like reengineering of mesoscale network models to predict the mode of action of tyrosine kinase inhibitors, antibody-drug conjugate-based therapeutic approaches, new virtual screening strategies and methodologies, three-dimensional culture systems for determining anticancer drug effects, integration of computer-aided drug design with network analysis for functional genomic studies have been recently applied in cancer researches to determine the drug-target interactions and discover the new targets (Olgen, 2018). It takes many years for a new drug to be approved by the FDA after in vitro and in vivo research and clinical trials. Due to the complexity of cancer, clinical trials of anticancer drugs take, on average, 1.5 years longer than other drugs (Kunnumakkara et al., 2019). The use of computational methods to complete this process in a shorter time and for appropriate drug design and synthesis has recently received increasing attention. Hence, computational methods play a critical role in drug discovery and are gaining popularity and success because of the ability to develop physical and chemical models by simulating bio molecular processes and discover the robust molecule before it is synthesized.

The quinone moiety is one of the most important structures in drug discovery and found in numerous natural products. Especially aminoquinones are accepted as pharmacological active substances due to their anticancer (Brandy et al., 2012) (Wellington et al., 2019), antibacterial (Jordão et al., 2013) (Janeczko et al., 2016), antifungal (Ryu et al., 2014) (Glamočlija et al., 2018), antiviral (Sendl et al., 1996), antimalarial (Belorgey et al., 2013) and antitubercular (Dey et al., 2014) activities. Thymoquinone (TQ) analogues have been reported to have anti-cancer effects on pancreatic (Banerjee et al., 2010) and ovarian cancer (Johnson-Ajinwo et al., 2018) cell lines. Bayrak et al. synthesized Plastoquinone analogs as a class of anticancer agents and examined their anticancer effects (Bayrak et al., 2020) (Bayrak et al., 2019) (Ciftci et al., 2019).

Therefore, in this study, a set consisting of 39 compounds that are in the literature (Bayrak et al., 2020) (Bayrak et al., 2019) (Ciftci et al., 2019) and carrying Plastoquinone analogues was investigated. Using the experimental activity values of these ligands reported in literature, a Field-based 3D-QSAR study and pharmacophore modeling was performed. Molecular docking study was performed to investigate the interactions with the 1IEP protein and the best scores were determined among the investigated ligands. Finally, since charge distribution is an important factor in protein-ligand interactions, the electrical charge properties of some ligands were investigated by different methods.

2. Materials and Methods

Chlorinated plastoquinone (PQ) analogs (Bayrak et al., 2020), aniline containing alkoxy group(s) PQ analogues (Bayrak et al., 2019) and amino-1,4-benzoquinone series (Ciftci et al., 2019) have been synthesized and, biological and anti-cancer activities were reported by Bayrak et al. In these studies, in the literature, a set of 39 ligands were selected by eliminating ligands whose activity values are not significant. For better comparison and linear arrangement, the inhibitory potencies of 39 compounds in the experimental data set, given as molar values (IC_{50}), were converted into pIC_{50} values ($pIC_{50} = 6 - \log_{10} IC_{50}$). The activities of the investigated ligands ranged from 4.64 to 6.04 (pIC_{50}). The compounds were drawn in 2D sketcher module of Maestro program package (Schrödinger Release, 2020) and then converted into 3D. The most important step of the pharmacophore model is to determine the appropriate training set, because this directly determines the quality of the generated pharmacophore. To build the 3D-QSAR model, the data set was divided in the ratio of 80:20. 27 compounds from data set were randomly selected as training set and remaining 12 compounds were used as test set, in considering with structural characteristics and biological activities. The energy minimization of compounds was performed by LigPrep (Schrödinger Release: LigPrep, 2020) module of Maestro software. The 3D-QSAR model was build using the Partial Least Square (PLS) regression analysis, the grid spacing was kept at 1 Å and 5 PLS factors were included in the model development. PHASE (Pharmacophore alignment and

scoring engine) (Schrödinger Releae: Phase, 2020) which is an effective instrument for the superposition of flexible ligands (Miller et al., 1999), was used to create pharmacophore and 3D-QSAR models. The spatial arrangements of functional groups that are typical and necessary for the biological activity of the ligands used in the study can be defined by PHASE (Evans et al., 2007). Ligands with experimental pIC50 values greater than 5.6 were designated as actives and < 4.8 as inactives, and the remaining compounds not meeting these breakpoints were considered moderately active. To generate the three-dimensional coordinates for all ligands, LigPrep was used (Schrödinger Release: LigPrep, 2020). The Epik (Greenwood et al., 2010) (Shelley et al., 2007) (Schrödinger Release: Epik, 2020), which is based on the more accurate Hammett and Taft methodologies was applied to generate the ionization/tautomeric states. The 1IEP protein was obtained from Protein Data Bank (Bernstein et al., 1977) (Berman et al., 2000). The Protein Preparation Wizard (PrepWizard) in Maestro was used to prepare the protein 1IEP following the steps outlined in Ref (Madhavi Sastry et al., 2013) but OPLS3e (Harder et al., 2016) was used as the force field. The docking analysis was done basing on creation of a receptor grid using the extra precision (XP) docking protocol in Glide (Schrödinger Release: Glide, 2020), after the protein preparation and specify the active binding sites of protein.

To elucidate the interactions between crystal molecules, Hirshfeld surface analysis was performed using the available *.cif files of the crystals by Crystal Explorer 3.1 program package (Turner et al., 2017). To identify the the intermolecular interactions and electric charge characteristics of studied molecules, Molecular Electrostatic Potential (MESP), Frontier Molecular Orbital (FMO) and Mulliken Charge Analysis was performed. In order to carry out the aforementioned analyzes, first of all, it is necessary to determine the optimum geometry of each molecule at the minimum energy level. Density functional theoretical (DFT) calculations were performed at the B3LYP (Becke's three parameter Lee–Yang–Parr) (Lee et al., 1988) (Becke, 1988) /6-31G(d,p) level of theory and using the Gaussian 09 program package (Frisch et al., 2016) to obtain optimized geometries of each PQ molecule.

3.   Results and Discussion

3. 1 Field-Based 3D-QSAR and Pharmacophore Modeling

QSAR modeling is an effective tool as it explores and uses the relationship between chemical structure and biological action in the development of new drug candidates (Tropsha, 2010). The Field-Based QSAR is a tool similar to CoMFA/CoMSIA, used to create a model for the relationship between 3D properties of a number of aligned compounds and known activity values. However, the models are not actually equivalent to standard CoMFA and CoMSIA models and often-different names are used, such as Force Field for CoMFA-like models and Gaussian Field for CoMSIA-like models. The Force Field consists of a steric field based on the Lennard-Jones potential and an electrostatic field with a dielectric dependent on a $1/r^2$ dependent distance, while the Gaussian based potential consists of five fields, namely steric, electrostatic, hydrophobic, hydrogen bond acceptor (HBA) and hydrogen bond donor (HBD). In this study, Gaussian field-based was preferred to create the 3D-QSAR model.

The dataset was divided into two parts to form the randomly selected 27 compounds as training sets and the remaining 12 compounds as test sets. The structural properties of the compounds in these sets, the experimentally recorded biological activity values (both IC_{50} and pIC_{50}), the predicted activities generated by the created model and the predicted error between recorded and estimated activity values are given in Table 1. The conformers obtained by energy minimization were used in the alignment of molecules, as shown in Fig. 1. The 3D-QSAR model was constructed using Partial Least Square (PLS) regression analysis, keeping the grid spacing at 1 Å and including 5 PLS factors in the model development. PLS offers the below statistical measures; standard deviation of regression (SD) which is the root mean square (RMS) error in the fitted activity values, regression correlation coefficient (R^2) that indicates the variance in observed activities, R^2 scramble, stability, ratio of the model variance to the observed activity variance (Fisher test or F test or variance ratio), significance level of variance ratio (P value), root mean square error of test

set (RMSE), cross-validated correlation coefficient for the test set (Q^2) by leave one out (LOO) method and Pearson-r values. The best alignment-dependent and Gaussian field-based model was achieved with PLS factor 5. While the experimental and predicted biological activity values with PLS factor 5 are given in Table 1, Table 2 shows a summary of the statistical results obtained for this model. For the specified model, it can be seen in Fig. 2 that there is a linear correlation between the actual and predicted activity values of the training set compounds. As seen in Table 2, the percentage contribution of steric, electrostatic, hydrophobic and hydrogen bond donor (HBD) were 0.423, 0.074, 0.375 and 0.128, respectively whereas the no contribution was obtained for the hydrogen bond acceptor (HBA). The contour plot analysis of studied compounds is given in Fig. 3. The most remarkable contribution was found due to steric effect for the Plastoquinone analogs activity, followed by hydrophobic which means that for protein-ligand interactions, this means that the steric field is more important than the electrostatic groups. The green color represents the favorable steric field region in the steric contour map, and the unfavorable steric field region is usually shown in a different color, however, Fig. 3 (a) indicates that no such region was detected and a bulky-group may be added to the green-colored zone for a larger activity value. The distribution of positive and negative electrostatic regions is characterized by electrostatic contour map. Negative charges are displayed by red and positives by blue. Similarly, in the hydrophobic counter map, the colors show us the regions where these molecules are suitable (yellow) and unsuitable (white) for hydrophobic or lipophilic groups for better activity. Positive (dark red) and negative (purple) regions indicate that the activity will increase and decrease in the presence of HBD groups, respectively, in HBD contours. A quick look at the statistics of the model created for 3D-QSAR, it is seen that the R^2 value is 0.97 and the stability value is calculated as 0.82. While a value of 0.4 was found for Q^2, SD was obtained at 0.08, Pearson-r at 0.85 and R^2 CV that derived from the LOO cross-validation method at 0.75. Godoy-Castillo et al. (Godoy-Castillo et al., 2021) studied the potent inhibitory effect of 33 naphthoquinone derivatives on heat shock 90 protein using a method similar to that in this study. In the QSAR modeling, the variance was calculated as 97%,

the standard deviation was found to be 0.06, and the Q^2 was obtained as 0.71. Based on these statistical data, it was stated that the model resulted in sufficient statistical significance and acceptable predictive power. Acuna et al. (Acuña et al., 2018) reported statistical parameters of CoMFA model for 18 quinone derivatives as $r^2 = 0.99$ and $q^2 = 0.625$. In a study performed for 52 heterocyclic quinones (Shi et al., 2021) with three different 3D-QSAR models, r^2 was calculated as 0.93, 0.94 and 0.95 and q^2 was calculated as 0.75, 0.59 and 0.73 for each model.

In this study, ligands with recorded pIC_{50} values greater than 5.6 were determined as actives and those with < 4.8 as inactives, to generate pharmacophore and 3D-QSAR models, while the remaining compounds that did not meet these breakpoints were considered moderately active. A set of three pharmacophore features was built by PHASE: two hydrophobic (H), a hydrogen bond acceptor (A) and an aromatic ring (R). To test the reliability of the models, the enrichment report was also generated basing on the hypo score, enrichment factor (EF), ROC (Receiver operating characteristics area under the curve), BEDROC (Boltzmann-enhanced Discrimination Receiver Operator Characteristic area under the curve), AUAC (Area under the accumulation curve) and matches for the AHHR_3 which selected as the best pharmacophore model due to the highest scores, as shown in Table 3. While the distances and angles between the different regions of this model are given in Fig. 4, Fig. 5 displays the mapping of all chemical properties of this differential pattern on active and inactive compounds.
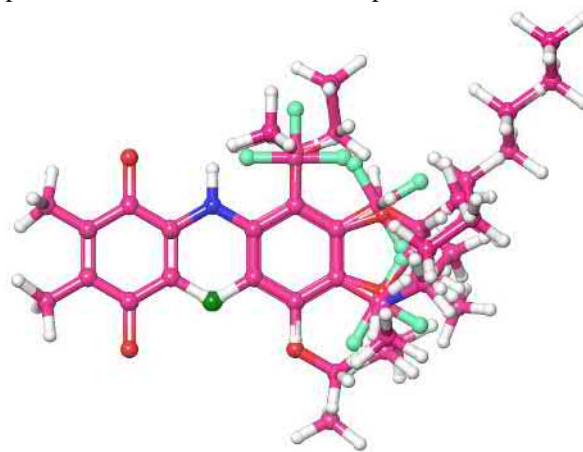
Figure 1. The alignment of 39 ligands used in dataset
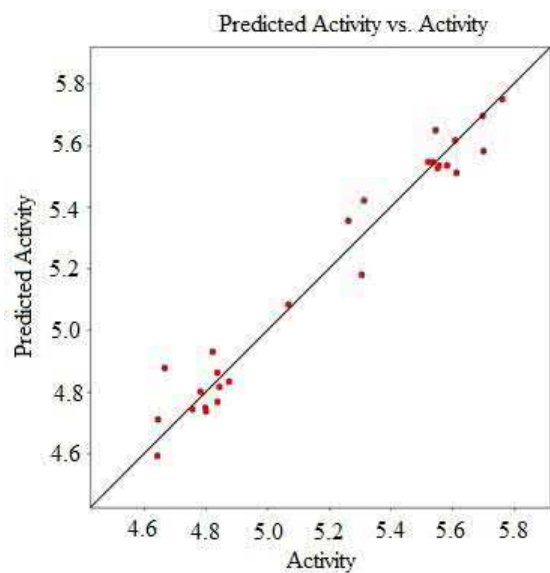
Figure 2. Scattered plots of experimental and predicted activity values for training set
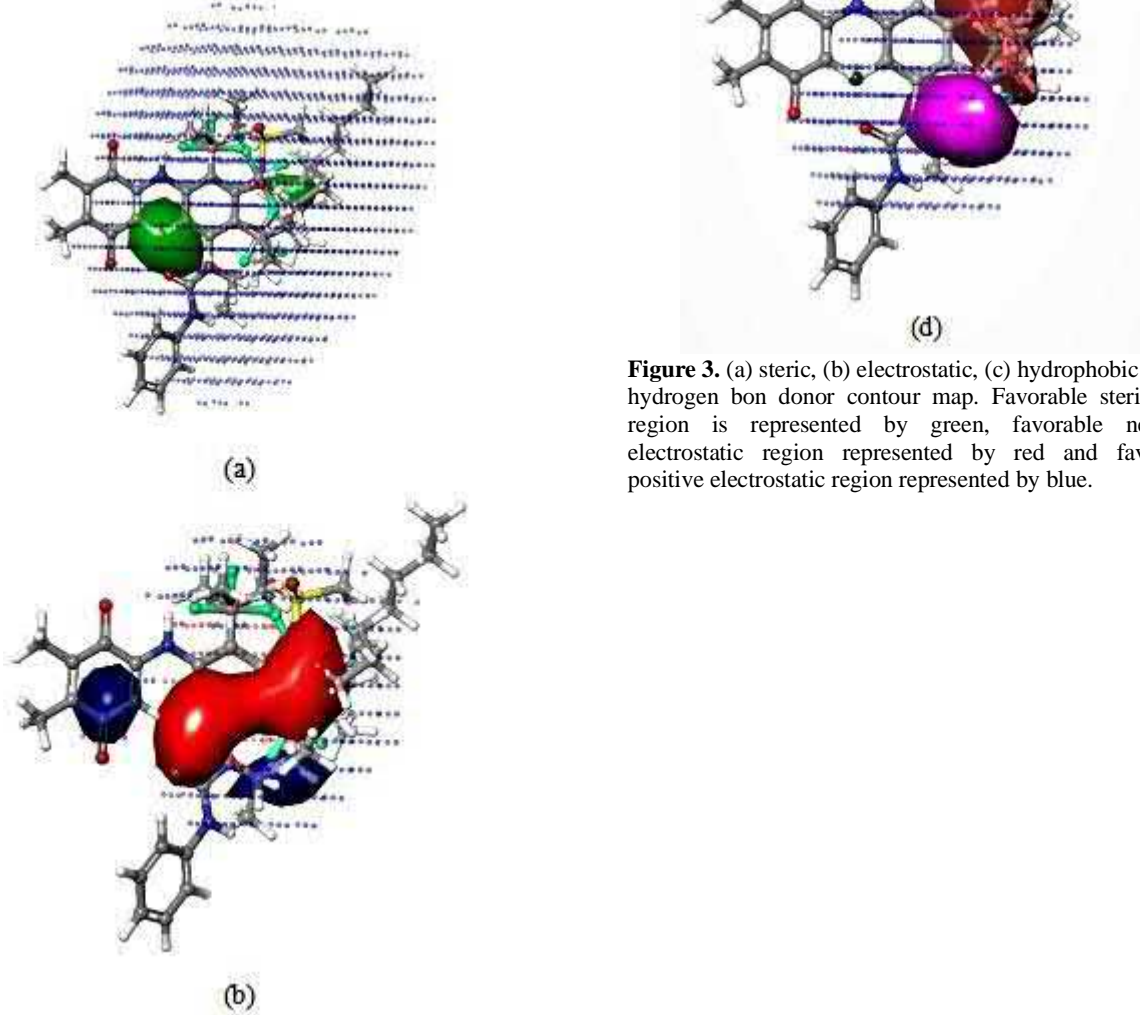
Figure 3. (a) steric, (b) electrostatic, (c) hydrophobic and (d) hydrogen bon donor contour map. Favorable steric field region is represented by green, favorable negative electrostatic region represented by red and favorable positive electrostatic region represented by blue.
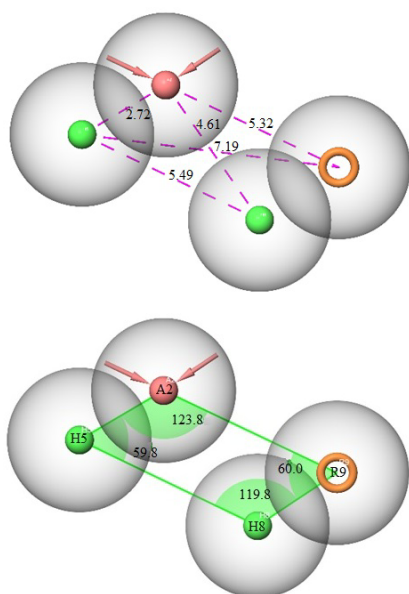
Figure 4. 3D-pharmacophore model with its corresponding chemical features for AHHR_3. (a) Intersite distances between the pharmacophoric points, (b) Intersite angles between the pharmacophoric points (A: Acceptor; H: Hydrophobic; R: Aromatic ring)

(a)

(b)

Figure 5. Mapping of the chemical features for active (a) and inactive (b) compounds onto the AHHR_3 pharmacophore model

3. 2 Ligand and Protein Preparation
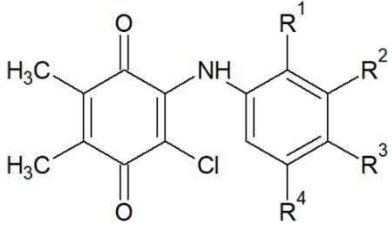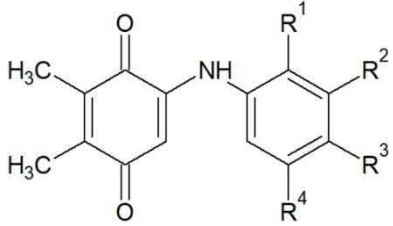
It is well known that to exploit the structure of protein-ligand or protein-protein binding sites is aimed in structure-based drug design. In ad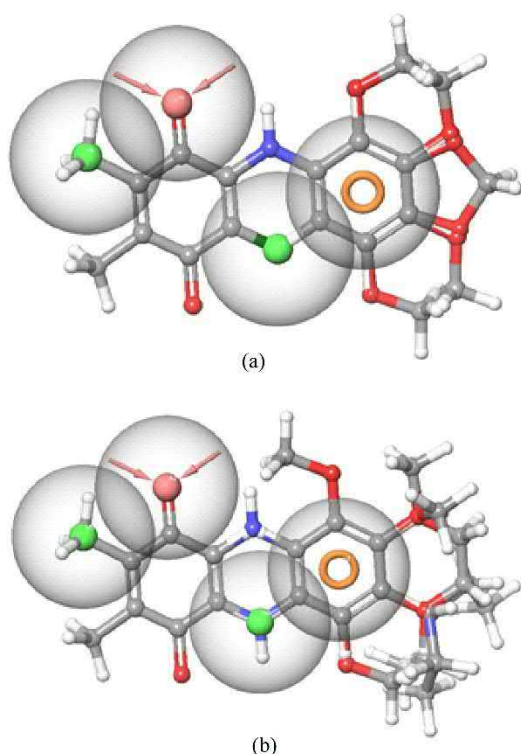dition, it is extremely important to know which binders or docking hits are complementary to the receptor in lead optimization. Hence, the prepared protein structure of 1IEP was uploaded into SiteMap, which generates various physiochemical properties (*Schrödinger Release: SiteMap*, 2020) (T. Halgren, 2007) (T. A. Halgren, 2009) and top five possible binding sites and determined their potential druggability were obtained. If the SiteScore value produced by software is 1.0 and above, it indicates a high druggability and this is used as a measure to define hydrophobicity, along with another value produced, DScore (Vidler et al., 2012). The generated scores for those sites are presented in Table 4. Although SiteScores obtained for sitemap, 4 and 5 are lesser than one, the difference is not much, and that means all binding pockets are having capability to bind different types of ligands. In this case, no binding pocket should be ignored, hence, all five sites (see Fig. 6) were handled for analysis. The region generated as sitemap 1 and 2 are accommodate the co-crystallized ligands for protein 1IEP (Nagar et al., 2002).

3. 3 Molecular Docking

One of the most widely used computational tools for the prediction of binding modes in protein-ligand interactions is molecular docking (Sousa et al., 2013). An accurate and comprehensive understanding of molecular interaction/recognition and knowledge of structural data as well as molecular protein-ligand binding mechanisms are of great importance for drug design, development, and discovery (Du et al., 2016). Docking analysis was performed after preparation of the protein and identification of active binding sites of the protein, as mentioned above. Docking analysis was performed by applying the extra precision (XP) docking protocol to the creation of a receiver grid. The co-crystallized ligands are also included for comparison of experimental and docked pose of the ligand, and given in Fig. 7. The RMSD values were obtained as 0.3669 Å, 0.5535 Å for sitemap 1 and 2, respectively. RMSD values up to 2 Å are accepted for

Table 1. The evaluated data set with their activity, classification and predicted activity by the Field-based 3D-QSAR model.

ABQ series and AQ11-17

PQ series and AQ1-9

	R^1	R^2	R^3	R^4	IC$_{50}$, µM	pIC$_{50}$	Predicted activity*	Predicted error	Dataset
ABQ1	OCH$_3$	H	H	H	2.78	5.56	5.56	0.00	training
ABQ2	H	OCH$_3$	H	H	2.01	5.70	5.63	-0.06	training
ABQ3	H	H	OCH$_3$	H	1.51	5.82	5.45	-0.37	test
ABQ4	OCH$_2$CH$_3$	H	H	H	2.81	5.55	5.57	0.02	training
ABQ5	H	OCH$_2$CH$_3$	H	H	2.84	5.55	5.66	0.12	test
ABQ6	H	H	OCH$_2$CH$_3$	H	2.01	5.70	5.35	-0.35	test
ABQ7	H	H	O(CH$_2$)$_3$CH$_3$	H	2.44	5.61	5.57	-0.05	training
ABQ8	H	H	O(CH$_2$)$_5$CH$_3$	H	4.95	5.31	5.35	0.05	training
ABQ9	H	H	O(CH$_2$)$_7$CH$_3$	H	5.47	5.26	5.33	0.07	test
ABQ10	OCH$_3$	H	OCH$_3$	H	4.86	5.31	5.49	0.17	training
ABQ11	OCH$_3$	H	H	OCH$_3$	0.92	6.04	5.53	-0.50	test
ABQ12	H	OCH$_3$	OCH$_3$	H	1.99	5.70	5.56	-0.14	training
ABQ13	H	OCH$_3$	H	OCH$_3$	2.85	5.55	5.61	0.07	training
ABQ14	OCH$_2$CH$_3$	H	H	OCH$_2$CH$_3$	3.00	5.52	5.55	0.02	test
ABQ15	H	OCH$_2$O		H	1.73	5.76	5.73	-0.03	training
ABQ16	H	O CH$_2$CH$_2$O		H	2.60	5.59	5.58	-0.01	test
ABQ17	H	OCH$_3$	OCH$_3$	OCH$_3$	2.62	5.58	5.54	-0.04	training
AQ1	H	H	H	H	13.38	4.87	4.78	-0.09	training
AQ2	CF$_3$	H	H	H	15.89	4.80	4.72	-0.08	training
AQ6	H	H	CH$_3$	H	16.55	4.78	4.74	-0.04	training
AQ7	CH(CH$_3$)$_2$	H	H	H	15.59	4.81	4.37	-0.44	test
AQ9	H	H	N(CH$_2$CH$_3$)$_2$	H	17.53	4.76	4.78	0.02	training
AQ11	H	H	H	H	3.01	5.52	5.52	0.00	training
AQ12	H	CF$_3$	H	H	2.92	5.53	5.54	0.00	training
AQ13	H	H	CF$_3$	H	5.48	5.26	5.29	0.02	training
AQ14	H	CH$_3$	H	H	2.29	5.64	5.56	-0.08	test
AQ15	H	H	CH$_3$	H	2.34	5.63	5.49	-0.14	test
AQ16	CH(CH$_3$)$_2$	H	H	H	8.58	5.07	5.11	0.04	training
AQ17	H	H	CH(CH$_3$)$_2$	H	2.46	5.61	5.60	-0.01	Training
PQ2	H	OCH$_3$	H	H	7.72	5.11	4.89	-0.22	test
PQ3	H	H	OCH$_3$	H	22.75	4.64	4.71	0.06	training
PQ5	H	OCH$_2$CH$_3$	H	H	8.95	5.05	4.92	-0.13	test
PQ6	H	H	OCH$_2$CH$_3$	H	22.79	4.64	4.61	-0.03	training
PQ9	OCH$_3$	H	H	OCH$_3$	14.57	4.84	4.79	-0.05	training
PQ10	H	OCH$_3$	OCH$_3$	H	14.57	4.84	4.82	-0.02	training
PQ11	H	OCH$_3$	H	OCH$_3$	15.07	4.82	4.87	0.04	training
PQ12	OCH$_2$CH$_3$	H	H	OCH$_2$CH$_3$	15.95	4.80	4.80	0.00	training
PQ14	H	OCH$_2$CH$_2$CH$_3$	H		21.65	4.66	4.84	0.17	training
PQ15	H	OCH$_3$	OCH$_3$	OCH$_3$	14.39	4.84	4.80	-0.05	Training

* Predicted activity for PLS factor 5

Table 2. The statistical values obtained by PLS factor 5.

SD	R^2	R^2 CV	R^2 Scramble	Stability	F	P	RMSE	Q^2	Pearson-r
0.0772	0.9699	0.7516	0.5976	0.824	135.4	$3.07.10^{-15}$	0.26	0.3993	0.8456

Steric		Electrostatic		Hydrophobic		H-bond Acceptor		H-bond Donor
0.423		0.074		0.375		0.128		0

Table 3. Enrichment report for the pharmacophore model which has the highest score (AHHR_3)

Hypothesis	Phase Hypo Score	EF	BEDROC	ROC	AUAC	Total Actives	Ranked Actives	Matches
AHHR_3	1.29	60.3	0.69	0.6	0.76	5	3	4 of 4

EF: enrichment factor, ROC: Receiver operating characteristics area under the curve, BEDROC: Boltzmann-enhanced Discrimination Receiver Operator Characteristic area under the curve, AUAC: Area under the accumulation curve

Sitemap 1

Sitemap 2

Sitemap 3
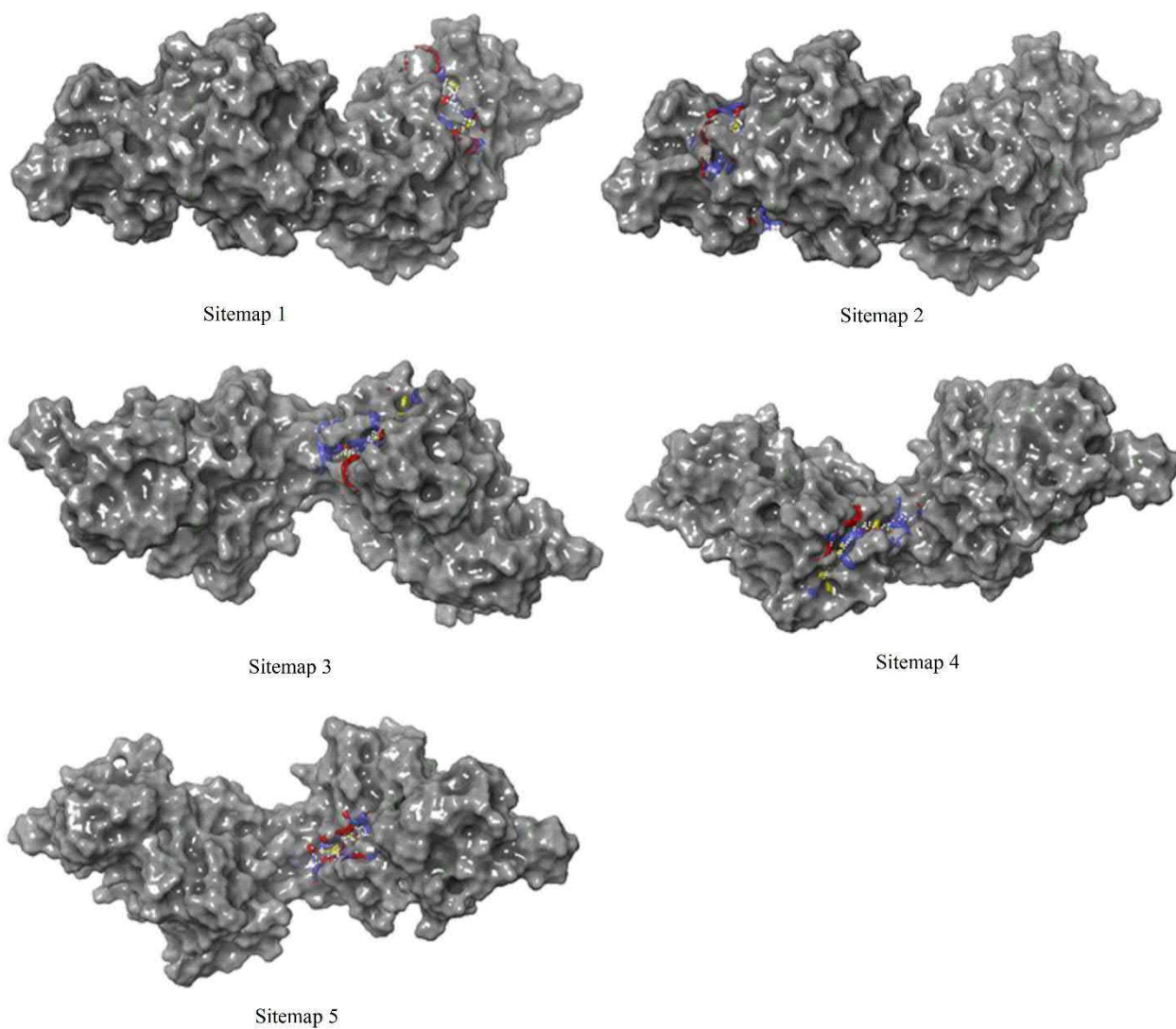
Sitemap 4

Sitemap 5

Figure 6. Top five possible binding sites of protein 1IEP

Table 4. Sitemap scoring analysis

	SiteScore	size	Dscore	volume
sitemap_1	1.093	327	1.113	848.925
sitemap_2	1.083	299	1.107	733.677
sitemap_3	1.034	100	1.073	197.568
sitemap_4	0.975	91	1.014	198.254
sitemap_5	0.891	70	0.819	203.056

molecular docking procedure, and in this study, low values were obtained for sitemap 1 and sitemap 2, which shows that the applied procedure is valid. Since the docking protocol is able to predict the binding for the crystal ligand correctly, the prediction for the rest of ligands will be also correct. The scores obtained from XP calculations for the sitemap-1 are presented in Table 5. DocScore (or GScore) refers to how good the interaction between drug and protein is, as the stability of docking between ligand and protein depends on the binding interaction. Docking scores are calculated as negative, and higher negative values of DocScore indicates the better binding affinity/interaction with the target protein/receptor (Bassyouni, 2017). As can be seen from table, docking score of the co-crystallized ligand was found to be -15.46, and the ABQ16 has the highest docking score with -9.55 among the studied ligands. Therefore, the interaction between 1IEP protein and this ligand are depicted in Fig. 8. 2D interaction diagram of ABQ16 ligand and protein is shown in Fig. 9 with comparison of co-crystallized ligand – protein interaction. Here, the co-crystalline ligand is located in the center and surrounds the residuals almost elliptical. Residuals in more inner elliptical orbits indicate direct contact, while those further out indicate indirect contact. In addition, the size of these elliptical orbits indicates the number of atomic contacts. In the inner orbit, we could find that the residue of TYR253 is important and has a pi-pi interaction with the aromatic ring (Fig. 9(b)). According to the docking studies analysis, hydrophobicity dominates the interactions, and the hydrophobic residues for ABQ16 ligand can be seen in Fig. 10. The hydrogen bond interaction is considered a vital parameter for the stability of the drug-protein complex and was calculated for all molecules with the best score in this study. For instance, the docking score of the AQ2, AQ6, ABQ11 and ABQ9 were obtained as 8.56, 8.2, 7.64 and 7.5, respectively with negative values. In addition, the

hydrogen bond values accompanying them were found to be 0.75, 1.26, 0.73 and 0.35, respectively as shown in Table 5. The results of the present study depicted that the studied Plastoquinone analogues showed good interactions with the 1IEP protein.
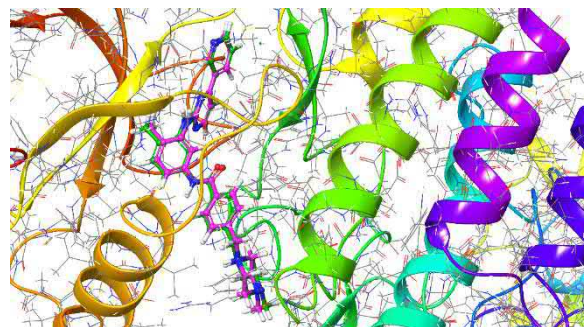
Figure 7. The comparison pose of experimental (magenta) and docked (green) co-crystallized ligand –for sitemap 1
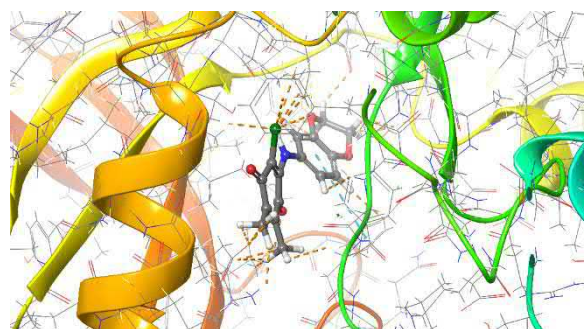
Figure 8. Interaction established between the 1IEP protein and ABQ16 ligand obtained through the docking protocol and for sitemap 1 (Hydrogen bonds were depicted as dashed lines in orange and blue dashed lines depict the pi-pi stacking).

A series of 1,4-naphthoquinone derivatives was synthesized and molecular docking was performed *in silico*. Among the 14 synthesized compounds, the highest docking score was obtained as -7.73, and hydrophobic interaction with LYS179 and TRP58 was reported (Ravichandiran et al., 2014). In the computational study to determine the interaction mechanism of the mono and dialkyloxy derivatives of 5,8-quinolinedione with the NQO1 enzyme, it was determined that the 5,8-quinolinedione moiety was bound to the enzyme via hydrophobic interactions and by aromatic residues Trp 105, Tyr 128 and Phe 178 (Kadela-Tomanek et al., 2017). In the study performed by placing 52 heterocyclic quinone

inhibitors in the active site of the NQO1 enzyme, it was determined that most compounds showed π stacking interactions with Trp105, Phe106 and Phe178 (López-Lira et al., 2018).
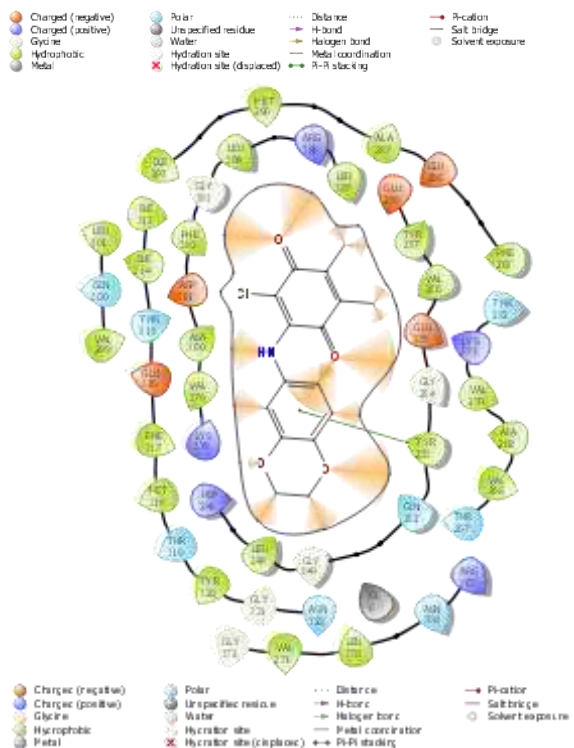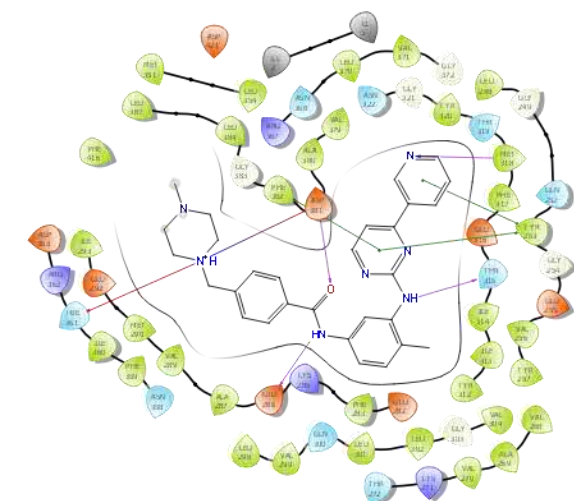
Figure 9. 2D co-crystallized ligand – protein (top), and ABQ16 ligand – protein (bottom) interaction diagram
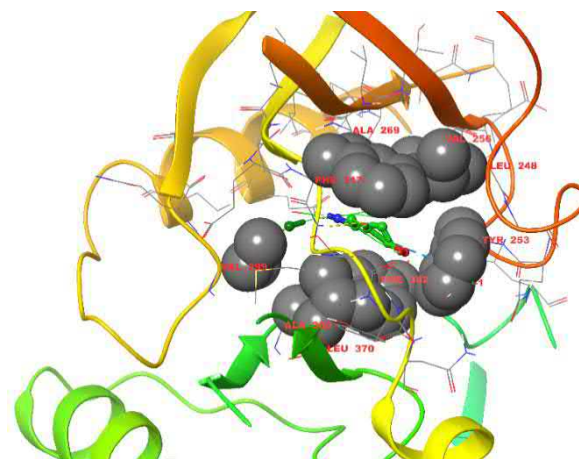
Figure 10. Hydrophobic residues

3. 4 Hirshfeld Surface and MESP Analysis

It is well known that the strength of the interaction between an inhibitor molecule and the specific target identified depends on the chemical characteristics -specifically charge properties- as well as the unique structure of the molecule. Hence, to determine the important interactions Hirshfeld surface and molecular electrostatic potential analysis were done and evaluated. The Hirshfeld surface is defined as the area occupied by a molecule in a crystal by partitioning the crystal electron density into molecular fragments (Spackman & Jayatilaka, 2009) (Spackman & Byrom, 1997). The Hirshfeld surface for a molecule is obtained by scanning van der Waals distances and defining interaction sites (Hirshfeld, 1977). When the Hirshfeld surface is obtained, the parameters d_e, which expresses the distance from Hirshfeld's surface to the nearest nucleus outside the surface, and d_i, which expresses the distance corresponding to the nearest nucleus on the surface, are defined. The normalized contact distance (d_{norm}), which enables the identification of regions of particular importance for intermolecular interactions, is defined as follows, depending on the d_e, d_i, and vdw radii of the atom (Spackman & McKinnon, 2002).

$$d_{norm} = \frac{d_i - r_i^{vdw}}{r_i^{vdw}} + \frac{d_e - r_e^{vdw}}{r_e^{vdw}}$$

Table 5. Docking scores obtained by XP visualizer for sitemap-1

Ligand	GScore	DockScore	LipophilicEvdW	PhobEn	PhobEnHB	PhobEnPairHB	HBond	Electro	Sitemap	PiCat	LowMW	Penalties	HBPenal	ExposPenal	RotPenal
1IEP-ligand1	-15.46	-15.46	-7.17	-2.53	-1.5	0	-1.84	-0.89	-0.33	0	0	0.03	0	0	0.29
1IEP-ligand2	-15.46	-15.46	-7.17	-2.53	-1.5	0	-1.84	-0.89	-0.33	0	0	0.03	0	0	0.29
ABQ16	-9.55	-9.55	-4.63	-2.25	-1	0	-0.53	-0.26	-0.61	0	-0.43	0	0	0	0.16
AQ2	-8.56	-8.56	-4.07	-1.74	0	0	-0.75	-0.57	-1.1	0	-0.5	0	0	0	0.18
AQ6	-8.2	-8.2	-3.47	-1.84	-1	0	-1.26	-0.44	-0.8	0	-0.5	0.86	0	0	0.26
ABQ11	-7.64	-7.64	-4.28	-1	0	0	-0.73	-0.65	-0.71	0	-0.43	0	0	0	0.15
ABQ9	-7.5	-7.5	-5.59	-1.6	0	0	-0.35	-0.03	-0.35	0	-0.2	0.12	0	0	0.49
AQ1	-7.44	-7.44	-4.35	-1.66	0	0	-0.36	-0.12	-0.73	0	-0.5	0	0	0	0.28
ABQ8	-7.14	-7.14	-5.27	-1.32	0	0	-0.35	-0.01	-0.33	0	-0.29	0	0	0	0.44
AQ7	-6.67	-6.67	-4.67	-1.19	0	0	-0.7	-0.13	-0.68	0	-0.5	1	0	0	0.21
ABQ5	-6.2	-6.2	-4.6	-1.37	0	0	-1.33	-0.37	-0.66	0	-0.48	2.35	0	0	0.25
ABQ10	-6.19	-6.19	-4.95	-0.45	0	0	-0.7	-0.1	-0.72	0	-0.43	1	0	0	0.15
ABQ14	-6.1	-6.1	-5.11	-0.45	0	0	-0.65	-0.13	-0.7	0	-0.33	1	0	0	0.27
ABQ7	-5.87	-5.87	-4.19	-0.85	0	0	-0.35	-0.07	-0.41	0	-0.39	0.02	0	0	0.36
ABQ6	-5.76	-5.76	-4.8	0	0	0	0	-0.12	-0.62	0	-0.48	0	0	0	0.25
ABQ12	-5.6	-5.6	-3.56	-0.62	0	0	-0.59	-0.28	-0.27	0	-0.43	0	0	0	0.15
ABQ15	-5.6	-5.6	-4.23	-0.86	0	0	-1.33	-0.16	-0.65	0	-0.48	1.95	0	0	0.17
AQ9	-5.5	-5.5	-4.36	0	0	0	-0.32	-0.16	-0.52	0	-0.5	0.1	0	0	0.26
ABQ17	-5.43	-5.43	-3.48	-0.57	0	0	-0.57	-0.46	-0.33	0	-0.33	0	0	0.18	0.13
ABQ13	-3.33	-3.33	-2.41	-0.12	0	0	-0.51	-0.09	-0.21	0	-0.43	0.01	0	0.27	0.15

GScore & DockScore: Docking Score; LipophilicEvdW: ChemScore lipophilic pair term and fraction of the total protein-ligand van der Waals energy; PhobEn: hydrophobic enclosure reward; PhobEnHB: reward for hydrophobically packed H-bond; PhobEnPairHB: eward for hydrophobically packed correlated H-bond; HBond: ChemScore H-bond pair term; Electro: electrostatics reward; Sitemap: sitemap ligand/receptor non H-bonding polar/hydrophobic and hydrophobic/hydrophilic complementarity terms; PiCat: reward for pi-cation interaction; LowMW: reward for ligands with low molecular weight; Penalties: polar atom burial and desolvation penalties, and penalty for intra-ligand contacts; HBPenal: penalty for ligands with large hydrophobic contacts and low H-bond scores; ExposPenal: Penalty for exposed hydrophobic ligand group; RotPenal: Rotatable bond penalty.

The 3D Hirshfeld surfaces of ABQ10, ABQ14, ABQ17, AQ9, AQ11, AQ17, PQ11 and PQ14 were obtained and illustrated in Fig. 6 showing surfaces that have been mapped over d_{norm}. Here, the red dots show the stronger hydrogen bonds. The d_{norm} region for each molecule is given in the Amstrong (Å) unit below the corresponding surface in Table 6. The O-H interactions can be seen in the Hirshfeld surface as bright red dots and the C-H···O interactions in light red spots, here as the H···H contacts are represented with the other visible spots on the surface. To highlight the close contacts of certain pairs of atoms, for example H-H, O-H/H-O and C-H/H-C, a 2D fingerprint plot of the surfaces is presented in Table 7 comprising the partial contribution of the whole surface. When one molecule is acceptor ($d_e < d_i$) and another is donor ($d_e > d_i$), it is observed as complementary regions in the fingerprint graph. The two sharp spikes in the third column of Table 7 indicate this, and show the typical O-H···O interaction. The contribution of this interaction to the total surface is over 25% for PQ11, PQ14, ABQ10 and ABQ17 molecules. H-H interactions are given in the second column of Table 7 and when their percentage ratios are considered, it is seen that they are the most dominant interactions. 2D fingerprint graphs for C-H /H-C interactions are in the fourth column. When the graphs are examined carefully, some of them have distinct "wings" and this corresponds to the C–H···π interactions (Spackman & Byrom, 1997) (McKinnon et al., 1998). In these wings, $d_e > d_i$ states correspond to the surface points around the C-H donor, while $d_e < d_i$ states correspond to the surface points around the π acceptor (Seth et al., 2011). The partial contribution of C–H···C interactions of the molecules were predicted as 11.6 %-18.4%.

The Molecular Electrostatic Potential (MESP) map is another important tool in studying intermolecular interactions in a molecular system and identifying nucleophilic and electrophilic attack localizations. These maps characterize the extremely negative to the extremely positive regions of the studied structure with colors starting from red to dark blue. Therefore, yellow color corresponds to a less negative region, while light blue indicates less positive region. The green color can be considered approximately as the neutral zone. The MESP surfaces of investigated molecules are represented in Table 6 to consider with

the Hirshfeld surfaces. The prominent colors on the maps are located around Oxygen atoms in the form of yellow-orange. This region, which indicates O-H···O interactions, is considered electronegative in accordance with the Hirshfeld surface. On the other hand, the absence of dark blue color on the maps means that there are no overly positive regions.

3. 5 Frontier Molecular Orbital (FMO) and Mulliken Charge Analysis

FMO energy analyzes are frequently used to determine the activities of molecular systems in many different areas, including complex or very large molecular systems. The most important orbitals in a molecule are the frontier molecular orbitals, called highest occupied molecular orbital (HOMO) and lowest unoccupied molecular orbital (LUMO), which determine the way the molecule interacts with other species. From these orbitals, HOMO characterizes electron donating ability, LUMO electron accepting ability, and the energy gap ($\Delta E = E_{LUMO} - E_{HOMO}$) between both characterizes molecular chemical stability. The energy gap is a critical parameter in determining electrical transport properties because it is largely responsible for the chemical and spectroscopic properties of molecules, as well as an indicator of electron conductivity (Atkins, 2001). As can be seen from Table 5, the first four ligands with the highest Docking Score among the studied molecules are ABQ16, AQ2, AQ6 and ABQ11. Therefore, HOMO and LUMO orbitals obtained with B3LYP/6-31G(d,p) level of theory for these ligands are shown in Fig. 11 together with their energy values and inter-orbital energy gaps. Once the HOMO and LUMO energy values of a molecule or molecular system are obtained, these values can be used to compute the other important parameters such as ionization potential, electron affinity, chemical hardness and softness, electronegativity, electronic chemical potential and electrophilic index which is expressed as the tendency of a molecule as a whole to accommodate electrons (Consonni & Todeschini, 2009). The formulas used in the calculation of the mentioned parameters and the results for each examined molecule, are listed in Table 8. A quick look at results, it can be seen that the frontier molecular energy levels of the examined structures, the energy differences between these levels and other

calculated parameters are very close to each other. When ABQ16 and ABQ11 and AQ2 and AQ6 are compared among themselves, it is seen that the results are much closer. For example, when looking at the results calculated for the *electrophilicity index*, larger values were obtained for ABQ compounds than for AQ compounds. This can be explained as, since these molecules have electronegative atoms, they increase their ability to accommodate electrons. While a similar effect is observed for *chemical softness*, the opposite is true for *chemical hardness* as expected. In addition, when the calculated energy values and the obtained molecular orbitals are evaluated together, it can be seen that the dominant electron transfer of these structures can be assigned as $\pi\rightarrow\pi^*$.

Mulliken Population Analysis is frequently used in theoretical calculations for the qualitative estimation of the partial atomic charges of a molecule. Mulliken charge affects many features of a molecular system such as dipole moment, polarizability, electronic structure etc. It quantifies how the electronic structure changes under atomic displacement, therefore, it is directly related to chemical bonds.

The net atomic charges of ABQ16, AQ2, AQ6 and ABQ11 molecules obtained by Mulliken population analysis are tabulated in Table 9. In Table 10, atomic Mulliken charges with the color index of each molecule are given and plotted. The atomic numbering in Table 9 was assigned according to the numbering given here. Based on the data in Table 9, it can be seen that the negative charge on the studied molecules is delocalized on the Oxygen atoms which bound to the ring with a double bound and on the bridging Nitrogen atom. Nitrogen atoms have a partial charge more than Oxygen atoms. While the Chlorine atoms in ABQ16 and ABQ11 molecules have a positive charge, the Mulliken charge of the Fluorine atoms in the AQ2 molecule is calculated as negative. All Hydrogen atoms have a positive charge while Carbon atoms have both negative and positive charge distribution.

4. *Conclusion*

In this study, a set of 39 ligands that activity values were determined experimentally and reported in the literature from the quinone family, which are known to be important structures in new drug design, were discussed. Since the training set had to be determined

appropriately for the pharmacophore modeling, 27 ligands were selected as training set and 12 ligands were selected as test set randomly. The 3D-QSAR study was performed using a field-based method and Partial Least Square (PLS) regression analysis, and the regression correlation coefficient (R^2) was obtained as approximately 0.97, and, it is understood that the estimated activity values are in good agreement with the experimental data. The generated receptor-guided alignment 3D-QSAR model has sufficient statistical significance and acceptable prediction power. When pharmacophore modeling was done, AHHR_3, which had three pharmacophore features, two hydrophobic (H), a hydrogen bond acceptor (A) and an aromatic ring (R), was determined as the model with the best scores. The enrichment report for the pharmacophore model of AHHR_3 was generated and the mapping of all chemical properties of differential pattern on active and inactive compounds was plotted. From the enrichment report, the EF, BEDROC, ROC and AUAC values are 60.3, 0.69, 0.6 and 0.76, respectively. Molecular docking study was carried out to determine the interactions between the ligands of interest and the 1IEP protein. In the preparation of ligand and protein for this study, it was seen that all five sites should be considered for analysis since the SiteScore of each site more than 1 or very close to 1. After docking operation, RMSD values were obtained as 0.3669 Å and 0.5535 Å for sites 1 and 2. Considering that the upper limit of the RMSD values is generally determined as 2 Å, it is seen that there is an extremely good agreement. By investigating the interactions of each ligand and 1IEP protein, ABQ16 ranked first with a DockScore of -9.55, followed by AQ2, AQ6 and ABQ11 with scores of -8.56, -8.2 and -7.64, respectively. The interaction between 1IEP protein and ABQ16 ligand was carried out in detail, and found that the residue of TYR253 is very important which has a pi-pi interaction with the aromatic ring of ligand. The electrical properties of the molecules which have high DScore were determined using the DFT (B3LYP) method. Studies for each of the four molecules show that there is no significant difference in the HOMO and LUMO energy values and the energy band differences between these orbitals. In addition, with the help of Hirshfeld surface analysis, the charge distributions of the molecules were examined and evaluated, and

element-based electronic bond interactions were examined with the 2D fingerprint plot.

References

ACUÑA, J., PIERMATTEY, J., CARO, D., BANNWITZ, S., BARRIOS, L., LÓPEZ, J., OCAMPO, Y., VIVAS-REYES, R., ARISTIZÁBAL, F., GAITÁN, R., MÜLLER, K., & FRANCO, L. (2018). Synthesis, Anti-Proliferative Activity Evaluation and 3D-QSAR Study of Naphthoquinone Derivatives as Potential Anti-Colorectal Cancer Agents. *Molecules 2018, Vol. 23, Page 186*, *23*(1), 186. https://doi.org/10.3390/MOLECULES2301018 6

ATKINS, P. W. (2001). *Physical Chemistry. The Extent of Adsorption*. Oxford University Press.

BANERJEE, S., AZMI, A. S., PADHYE, S., SINGH, M. W., BARUAH, J. B., PHILIP, P. A., SARKAR, F. H., & MOHAMMAD, R. M. (2010). Structure-activity studies on therapeutic potential of thymoquinone analogs in pancreatic cancer. *Pharmaceutical Research*, *27*(6), 1146–1158. https://doi.org/10.1007/S11095-010-0145-3/FIGURES/8

BASSYOUNI, F. (2017). *Molecular Modeling and Biological Activities of New Potent Antimicrobial, Anti-Inflammatory and Anti-Nociceptive of 5-Nitro Indoline-2-One Derivatives*. https://doi.org/10.4172/2169-0138.1000148

BAYRAK, N., YILDIRIM, H., YILDIZ, M., RADWAN, M. O., OTSUKA, M., FUJITA, M., CIFTCI, H. I., & TUYUN, A. F. (2020). A novel series of chlorinated plastoquinone analogs: Design, synthesis, and evaluation of anticancer activity. *Chemical Biology & Drug Design*, *95*(3), 343–354. https://doi.org/10.1111/CBDD.13651

BAYRAK, N., YILDIRIM, H., YILDIZ, M., RADWAN, M. O., OTSUKA, M., FUJITA, M., TUYUN, A. F., & CIFTCI, H. I. (2019). Design, synthesis, and biological activity of Plastoquinone analogs as a new class of anticancer agents. *Bioorganic Chemistry*, *92*, 103255. https://doi.org/10.1016/J.BIOORG.2019.10325 5

BECKE, A. D. (1988). Density-functional exchange-energy approximation with correct asymptotic

behavior. *Physical Review A*, *38*(6), 3098. https://doi.org/10.1103/PhysRevA.38.3098

BELORGEY, D., ANTOINE LANFRANCHI, D., & DAVIOUD-CHARVET, E. (2013). 1,4-Naphthoquinones and Other NADPH-Dependent Glutathione Reductase- Catalyzed Redox Cyclers as Antimalarial Agents. *Current Pharmaceutical Design*, *19*(14), 2512–2528.

BERMAN, H. M., WESTBROOK, J., FENG, Z., GILLILAND, G., BHAT, T. N., WEISSIG, H., SHINDYALOV, I. N., & BOURNE, P. E. (2000). The Protein Data Bank. *Nucleic Acids Research*, *28*(1), 235–242. https://doi.org/10.1093/NAR/28.1.235

BERNSTEIN, F. C., KOETZLE, T. F., WILLIAMS, G. J. B., MEYER, E. F., BRICE, M. D., RODGERS, J. R., KENNARD, O., SHIMANOUCHI, T., & TASUMI, M. (1977). The protein data bank: A computer-based archival file for macromolecular structures. *Journal of Molecular Biology*, *112*(3), 535–542. https://doi.org/10.1016/S0022-2836(77)80200-3

BRANDY, Y., ONONIWU, I., ADEDEJI, D., WILLIAMS, V., MOUAMBA, C., KANAAN, Y., COPELAND, R. L., WRIGHT, D. A., BUTCHER, R. J., DENMEADE, S. R., & BAKARE, O. (2012). Synthesis and cytotoxic activities of some 2-Arylnaphtho [2,3-d]oxazole-4,9-dione derivatives on androgen-dependent (LNCaP) and androgen-independent (PC3) human prostate cancer cell lines. *Investigational New Drugs*, *30*(4), 1709–1714. https://doi.org/10.1007/S10637-011-9635-3/TABLES/2

BRANNON-PEPPAS, L., & BLANCHETTE, J. O. (2004). Nanoparticle and targeted systems for cancer therapy. *Advanced Drug Delivery Reviews*, *56*(11), 1649–1659. https://doi.org/10.1016/J.ADDR.2004.02.014

CIFTCI, H. I., BAYRAK, N., YILDIRIM, H., YILDIZ, M., RADWAN, M. O., OTSUKA, M., FUJITA, M., & TUYUN, A. F. (2019). Discovery and structure–activity relationship of plastoquinone analogs as anticancer agents against chronic myelogenous leukemia cells. *Archiv Der Pharmazie*, *352*(12), 1900170. https://doi.org/10.1002/ARDP.201900170

CONSONNI, V., & TODESCHINI, R. (2009). *Molecular Descriptors for Chemoinformatics: Volume I: Alphabetical Listing/Volume II: Appendices, References*. John Wiley & Sons,

Ltd.

DEY, D., RAY, R., & HAZRA, B. (2014). Antitubercular and Antibacterial Activity of Quinonoid Natural Products Against Multi-Drug Resistant Clinical Isolates. *Phytotherapy Research*, *28*(7), 1014–1021. https://doi.org/10.1002/PTR.5090

DU, X., LI, Y., XIA, Y. L., AI, S. M., LIANG, J., SANG, P., JI, X. L., & LIU, S. Q. (2016). Insights into Protein–Ligand Interactions: Mechanisms, Models, and Methods. *International Journal of Molecular Sciences 2016, Vol. 17, Page 144*, *17*(2), 144. https://doi.org/10.3390/IJMS17020144

EVANS, D. A., DOMAN, T. N., THORNER, D. A., & BODKIN, M. J. (2007). 3D QSAR methods: Phase and catalyst compared. *Journal of Chemical Information and Modeling*, *47*(3), 1248–1257. https://doi.org/10.1021/CI7000082/ASSET/IMAGES/MEDIUM/CI7000082N00001.GIF

FRISCH, M. J., TRUCKS, G. W., SCHLEGEL, H. B., SCUSERIA, G. E., ROBB, M. A., CHEESEMAN, J. R., SCALMANI, G., BARONE, V., PETERSSON, G. A., NAKATSUJI, H., LI, X., CARICATO, M., MARENICH, A., BLOINO, J., JANESKO, B. G., GOMPERTS, R., MENNUCCI, B., HRATCHIAN, H. P., ORTIZ, J. V., … FOX, D. J. (2016). *Gaussian 09* (Revision A.02). Gaussian, Inc.

GLAMOČLIJA, U., PADHYE, S., ŠPIRTOVIĆ-HALILOVIĆ, S., OSMANOVIĆ, A., VELJOVIĆ, E., ROCA, S., NOVAKOVIĆ, I., MANDIĆ, B., TUREL, I., KLJUN, J., TRIFUNOVIĆ, S., KAHROVIĆ, E., PAVELIĆ, S. K., HAREJ, A., KLOBUČAR, M., & ZAVRŠNIK, D. (2018). Synthesis, Biological Evaluation and Docking Studies of Benzoxazoles Derived from Thymoquinone. *Molecules 2018, Vol. 23, Page 3297*, *23*(12), 3297. https://doi.org/10.3390/MOLECULES23123297

GODOY-CASTILLO, C., BRAVO-ACUÑA, N., ARRIAGADA, G., FAUNES, F., LEÓN, R., & SOTO-DELGADO, J. (2021). Identification of the naphthoquinone derivative inhibitors binding site in heat shock protein 90: an induced-fit docking, molecular dynamics and 3D-QSAR study. *Journal of Biomolecular Structure and Dynamics*, *39*(16), 5977–5987.

https://doi.org/10.1080/07391102.2020.1803134/SUPPL_FILE/TBSD_A_1803134_SM9783.PDF

GOTTESMAN, M. M. (2001). *MECHANISMS OF CANCER DRUG RESISTANCE*.

GREENWOOD, J. R., CALKINS, D., SULLIVAN, A. P., & SHELLEY, J. C. (2010). Towards the comprehensive, rapid, and accurate prediction of the favorable tautomeric states of drug-like molecules in aqueous solution. *Journal of Computer-Aided Molecular Design*, *24*(6–7), 591–604. https://doi.org/10.1007/S10822-010-9349-1/FIGURES/6

HALGREN, T. (2007). New Method for Fast and Accurate Binding-site Identification and Analysis. *Chemical Biology & Drug Design*, *69*(2), 146–148. https://doi.org/10.1111/J.1747-0285.2007.00483.X

HALGREN, T. A. (2009). Identifying and characterizing binding sites and assessing druggability. *Journal of Chemical Information and Modeling*, *49*(2), 377–389. https://doi.org/10.1021/CI800324M/ASSET/IMAGES/MEDIUM/CI-2008-00324M_0006.GIF

HARDER, E., DAMM, W., MAPLE, J., WU, C., REBOUL, M., XIANG, J. Y., WANG, L., LUPYAN, D., DAHLGREN, M. K., KNIGHT, J. L., KAUS, J. W., CERUTTI, D. S., KRILOV, G., JORGENSEN, W. L., ABEL, R., & FRIESNER, R. A. (2016). OPLS3: A Force Field Providing Broad Coverage of Drug-like Small Molecules and Proteins. *Journal of Chemical Theory and Computation*, *12*(1), 281–296. https://doi.org/10.1021/ACS.JCTC.5B00864/SUPPL_FILE/CT5B00864_SI_001.ZIP

HIRSHFELD, F. L. (1977). Bonded-atom fragments for describing molecular charge densities. *Theoretica Chimica Acta 1977 44:2*, *44*(2), 129–138. https://doi.org/10.1007/BF00549096

JANECZKO, M., DEMCHUK, O. M., STRZELECKA, D., KUBIŃSKI, K., & MASŁYK, M. (2016). New family of antimicrobial agents derived from 1,4-naphthoquinone. *European Journal of Medicinal Chemistry*, *124*, 1019–1025. https://doi.org/10.1016/J.EJMECH.2016.10.034

JOHNSON-AJINWO, O. R., ULLAH, I., MBYE, H., RICHARDSON, A., HORROCKS, P., & LI, W. W. (2018). The synthesis and evaluation of

thymoquinone analogues as anti-ovarian cancer and antimalarial agents. *Bioorganic & Medicinal Chemistry Letters*, *28*(7), 1219–1222. https://doi.org/10.1016/J.BMCL.2018.02.051

JORDÃO, A. K., NOVAIS, J., LEAL, B., ESCOBAR, A. C., DOS SANTOS JÚNIOR, H. M., CASTRO, H. C., & FERREIRA, V. F. (2013). Synthesis using microwave irradiation and antibacterial evaluation of new N,O-acetals and N,S-acetals derived from 2-amino-1,4-naphthoquinones. *European Journal of Medicinal Chemistry*, *63*, 196–201. https://doi.org/10.1016/J.EJMECH.2013.01.010

KADELA-TOMANEK, M., JASTRZĘBSKA, M., PAWEŁCZAK, B., BĘBENEK, E., CHROBAK, E., LATOCHA, M., KSIĄŻEK, M., KUSZ, J., & BORYCZKA, S. (2017). Alkynyloxy derivatives of 5,8-quinolinedione: Synthesis, in vitro cytotoxicity studies and computational molecular modeling with NAD(P)H:Quinone oxidoreductase 1. *European Journal of Medicinal Chemistry*, *126*, 969–982. https://doi.org/10.1016/J.EJMECH.2016.12.031

KUNNUMAKKARA, A. B., BORDOLOI, D., SAILO, B. L., ROY, N. K., THAKUR, K. K., BANIK, K., SHAKIBAEI, M., GUPTA, S. C., & AGGARWAL, B. B. (2019). Cancer drug development: The missing links. *Experimental Biology and Medicine*, *244*(8), 663–689. https://doi.org/10.1177/1535370219839163/AS SET/IMAGES/LARGE/10.1177_15353702198 39163-FIG2.JPEG

LEE, C., YANG, W., & PARR, R. G. (1988). Development of the Colle-Salvetti correlation-energy formula into a functional of the electron density. *Physical Review B*, *37*(2), 785. https://doi.org/10.1103/PhysRevB.37.785

LÓPEZ-LIRA, C., ALZATE-MORALES, J. H., PAULINO, M., MELLA-RAIPÁN, J., SALAS, C. O., TAPIA, R. A., & SOTO-DELGADO, J. (2018). Combined molecular modelling and 3D-QSAR study for understanding the inhibition of NQO1 by heterocyclic quinone derivatives. *Chemical Biology & Drug Design*, *91*(1), 29–38. https://doi.org/10.1111/CBDD.13051

MADHAVI SASTRY, G., ADZHIGIREY, M., DAY, T., ANNABHIMOJU, R., & SHERMAN, W. (2013). Protein and ligand preparation: Parameters, protocols, and influence on virtual screening enrichments. *Journal of Computer-Aided Molecular Design*, *27*(3), 221–234. https://doi.org/10.1007/S10822-013-9644-8/TABLES/9

MCKINNON, J. J., MITCHELL, A. S., & SPACKMAN, M. A. (1998). Hirshfeld surfaces: a new tool for visualising and exploring molecular crystals. *Chemistry–A European Journal*, *4*(11), 2136–2141.

MILLER, M. D., SHERIDAN, R. P., & KEARSLEY, S. K. (1999). SQ: A program for rapidly producing pharmacophorically relevent molecular superpositions. *Journal of Medicinal Chemistry*, *42*(9), 1505–1514. https://doi.org/10.1021/JM9806143/SUPPL_FI LE/JM9806143_S.PDF

NAGAR, B., BORNMANN, W. G., PELLICENA, P., SCHINDLER, T., VEACH, D. R., MILLER, W. T., CLARKSON, B., & KURIYAN, J. (2002). Crystal Structures of the Kinase Domain of c-Abl in Complex with the Small Molecule Inhibitors PD173955 and Imatinib (STI-571). *Biochemistry and Biophysics*, *62*(15), 4236–4243.

OLGEN, S. (2018). Overview on Anticancer Drug Design and Development. *Current Medicinal Chemistry*, *25*(15), 1704–1719. https://doi.org/10.2174/0929867325666171129 215610

RAVICHANDIRAN, P., PREMNATH, D., & VASANTHKUMAR, S. (2014). Synthesis, molecular docking and antibacterial evaluation of new 1,4-naphthoquinone derivatives contains carbazole-6,11-dione moiety. *Journal of Chemical Biology 2014 7:3*, *7*(3), 93–101. https://doi.org/10.1007/S12154-014-0115-Z

RYU, C. K., OH, S. Y., CHOI, S. J., & KANG, D. Y. (2014). Synthesis of Antifungal Evaluation of 2H-[1,2,3]Triazolo[4,5-g]isoquinoline-4,9-diones. *Chemical and Pharmaceutical Bulletin*, *62*(11), c14-00527. https://doi.org/10.1248/CPB.C14-00527

SCHRÖDINGER RELEAE: PHASE (NO. 4). (2020). Schrödinger, LLC.

SCHRÖDINGER RELEASE: EPIK (NO. 4). (2020). Schrödinger, LLC.

SCHRÖDINGER RELEASE: GLIDE, (NO. 4). (2020). Schrödinger, LLC.

SCHRÖDINGER RELEASE: LIGPREP (NO. 4). (2020). Schrödinger, LLC.

SCHRÖDINGER RELEASE: SITEMAP (NO. 4). (2020). Schrödinger, LLC.

SCHRÖDINGER RELEASE (NO. 4). (2020). Maestro, Schrödinger, LLC.

SENDL, A., CHEN, J. L., JOLAD, S. D., STODDART, C., ROZHON, E., KERNAN, M., NANAKORN, W., & BALICK, M. (1996). Two New Naphthoquinones with Antiviral Activity from Rhinacanthus nasutus. *Journal of Natural Products*, *59*(8), 808–811. https://doi.org/10.1021/NP9601871

SETH, S. K., MAITY, G. C., & KAR, T. (2011). Structural elucidation, Hirshfeld surface analysis and quantum mechanical study of para-nitro benzylidene methyl arjunolate. *Journal of Molecular Structure*, *1000*(1–3), 120–126. https://doi.org/10.1016/J.MOLSTRUC.2011.06.003

SHELLEY, J. C., CHOLLETI, A., FRYE, L. L., GREENWOOD, J. R., TIMLIN, M. R., & UCHIMAYA, M. (2007). Epik: A software program for pKa prediction and protonation state generation for drug-like molecules. *Journal of Computer-Aided Molecular Design*, *21*(12), 681–691. https://doi.org/10.1007/S10822-007-9133-Z/TABLES/5

SHI, J., LONG, T., ZHOU, Y., WANG, L., JIANG, C., PAN, D., & ZHU, X. (2021). Efficiency and Quantitative Structure-Activity Relationship of Monoaromatics Oxidation by Quinone-Activated Persulfate. *Frontiers in Chemistry*, *9*, 172. https://doi.org/10.3389/FCHEM.2021.580643/XML/NLM

SIEGEL, R. L., MILLER, K. D., & JEMAL, A. (2016). CANCER STATISTICS, 2016. *CA: A Cancer Journal for Clinicians*, *66*(1), 7–30. https://doi.org/10.3322/CAAC.21332

SOUSA, S. F., RIBEIRO, A. J. M., COIMBRA, J. T. S., NEVES, R. P. P., MARTINS, S. A., MOORTHY, N. S. H. N., FERNANDES, P. A., & RAMOS, M. J. (2013). Protein-Ligand Docking in the New Millennium – A Retrospective of 10 Years in the Field. *Current Medicinal Chemistry*, *20*(18), 2296–2314.

SPACKMAN, M. A., & BYROM, P. G. (1997). A novel definition of a molecule in a crystal. *Chemical Physics Letters*, *267*(3–4), 215–220. https://doi.org/10.1016/S0009-2614(97)00100-0

SPACKMAN, M. A., & JAYATILAKA, D. (2009). Hirshfeld surface analysis. *CrystEngComm*, *11*(1), 19–32. https://doi.org/10.1039/B818330A

SPACKMAN, M. A., & MCKINNON, J. J. (2002). Fingerprinting intermolecular interactions in molecular crystals. *CrystEngComm*, *4*(66), 378–392.

TROPSHA, A. (2010). Best Practices for QSAR Model Development, Validation, and Exploitation. *Molecular Informatics*, *29*(6–7), 476–488. https://doi.org/10.1002/MINF.201000061

TURNER, M., KINNON, J. M., S. WOLFF, GRIMWOOD, D., SPACKMAN, P., JAYATILAKA, D., & SPACKMAN, M. (2017). *CrystalExplorer17*. University of Western Australia.

VIDLER, L. R., BROWN, N., KNAPP, S., & HOELDER, S. (2012). Druggability analysis and structural classification of bromodomain acetyl-lysine binding sites. *Journal of Medicinal Chemistry*, *55*(17), 7346–7359. https://doi.org/10.1021/JM300346W/SUPPL_FILE/JM300346W_SI_002.PDF

WELLINGTON, K. W. (2015). *Understanding cancer and the anticancer activities of naphthoquinones-a review*. https://doi.org/10.1039/c4ra13547d

WELLINGTON, K. W., KOLESNIKOVA, N. I., NYOKA, N. B. P., & MCGAW, L. J. (2019). Investigation of the antimicrobial and anticancer activity of aminonaphthoquinones. *Drug Development Research*, *80*(1), 138–146. https://doi.org/10.1002/DDR.21477

Table 6. The Hirshfeld and Molecular Electronic Potential (MEP) Surfaces for the ligands that experimentally crystallographic structures are available
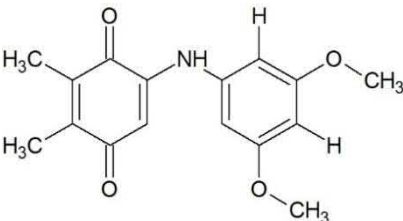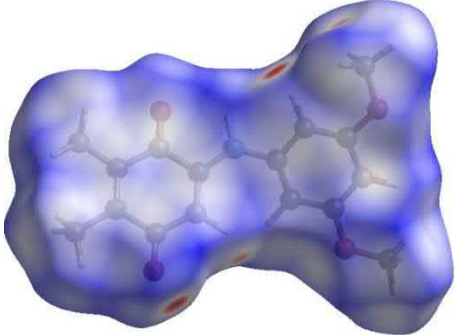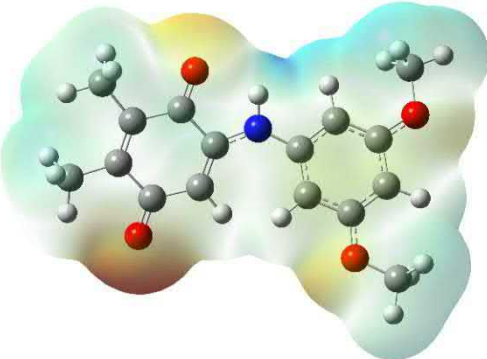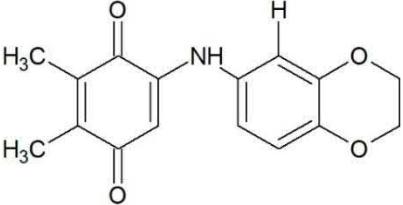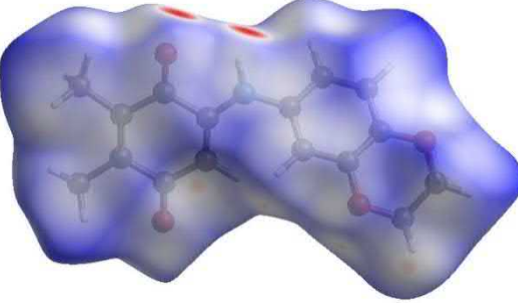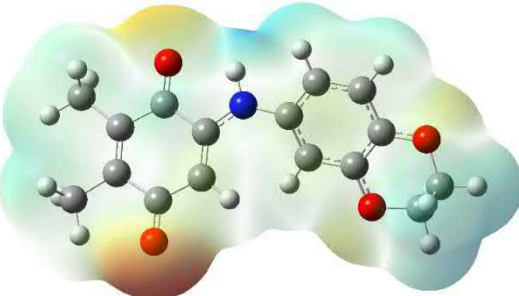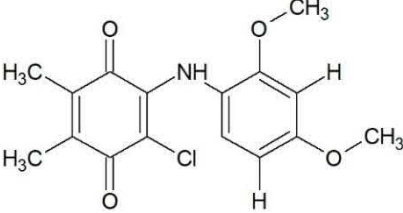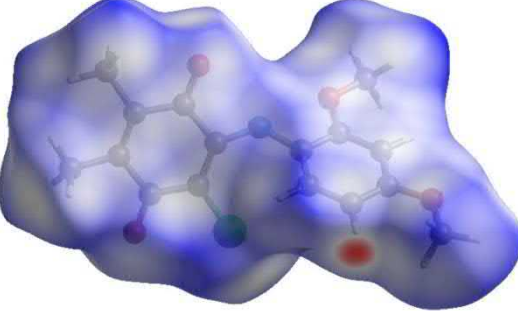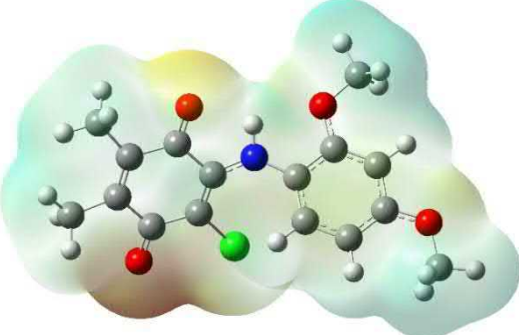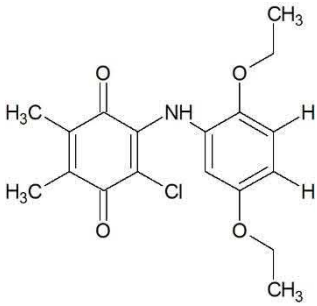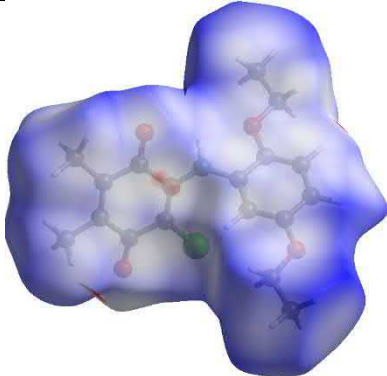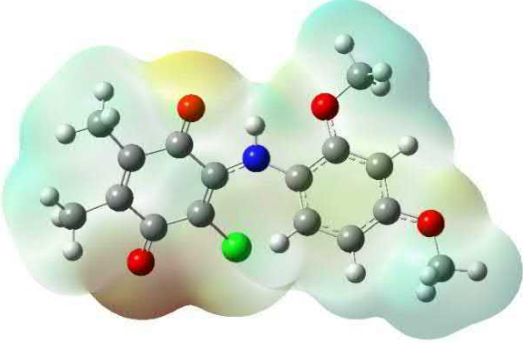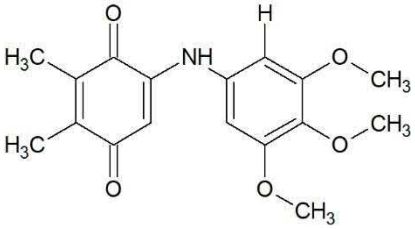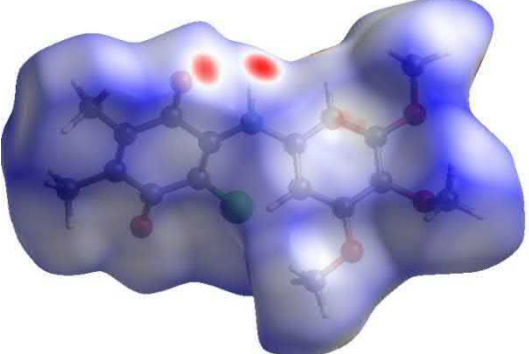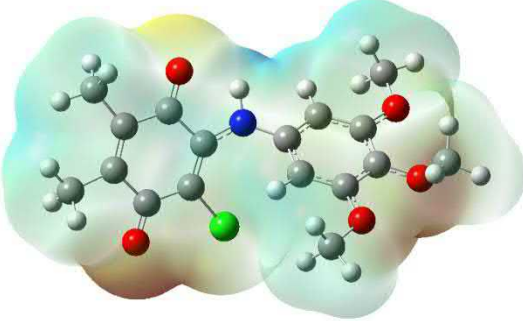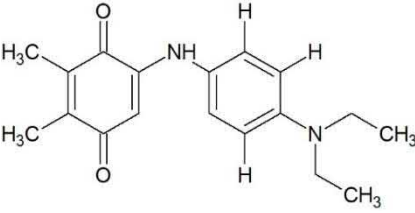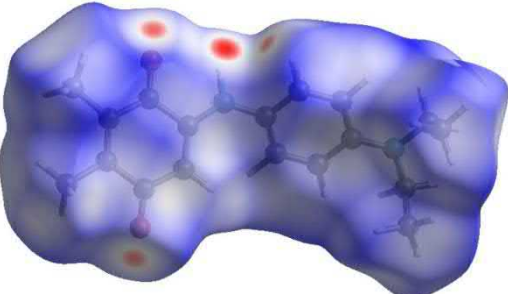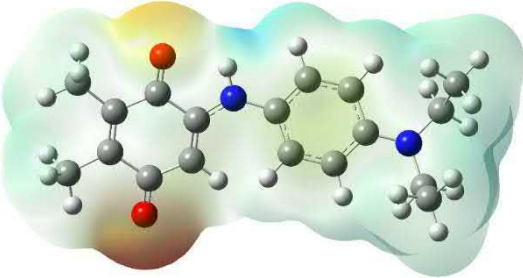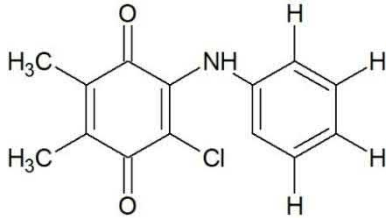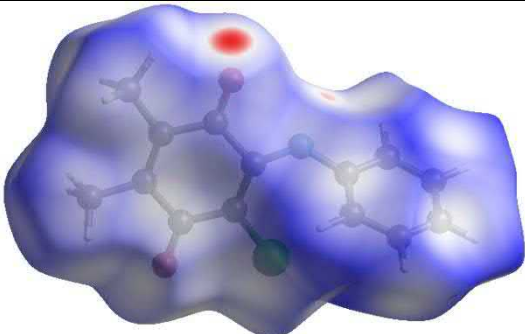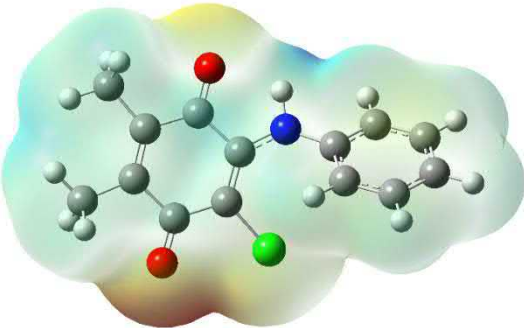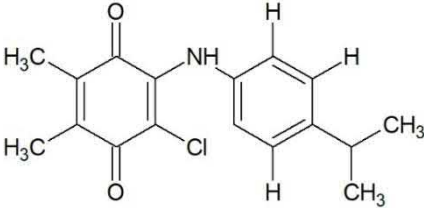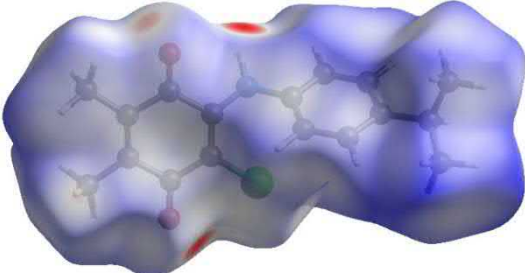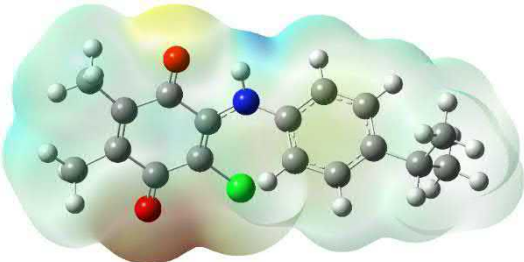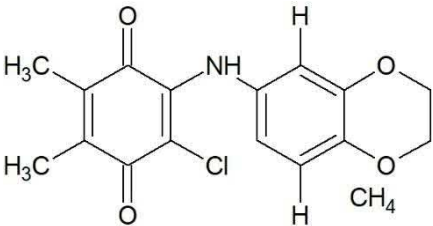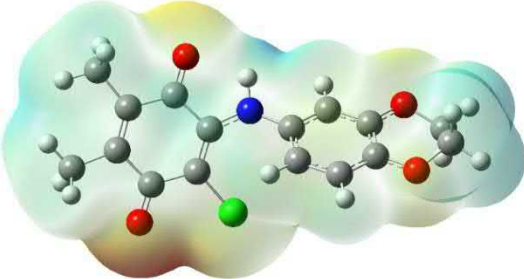
Ligand Name	Ligand Structure	Hirshfeld Surface (d_{norm})	Molecular Electrostatic Potential (MESP) Surface
PQ11		-0.1986 (red color) 1.1136 (blue color)	
PQ14		-0.2896 (red color) 1.3363 (blue color)	
ABQ10		-0.2598 (red color) 1.2592 (blue color)	

Table 6. Continued

Ligand Name	Ligand Structure	Hirshfeld Surface (d_{norm})	Molecular Electrostatic Potential (MESP) Surface
ABQ14		 -0.1566 (red color) 1.6257 (blue color)	
ABQ17		 -0.2367 (red color) 1.4253 (blue color)	
AQ9		 -0.2051 (red color) 1.3109 (blue color)	

Table 6. Continued

Ligand Name	Ligand Structure	Hirshfeld Surface (d_{norm})	Molecular Electrostatic Potential (MESP) Surface
AQ11		-0.1445 (red color) 1.1977 (blue color)	
AQ17		-0.3922 (red color) 1.5692 (blue color)	
ABQ16		*.cif file of molecule is not available	

Table 7. The 2D fingerprint histogram of the related compounds resolved into O···H, C···H and H···H contacts

Ligand Name	H-H	H-O/O-H	H-C/C-H
PQ11	H-H: 47.4%	H-O / O-H: 28.5 %	H-C / C-H: 11.6 %
PQ14	H-H: 44.4%	H-O / O-H: 29.2 %	H-C / C-H: 18.4 %
ABQ10	H-H: 32.4 %	H-O / O-H: 26.7 %	H-C / C-H: 16.2 %
ABQ14	H-H: 52.3 %	H-H / O-H: 18.1 %	H-C / C-H: 11.6 %

Table 7. Continued

Ligand Name	H-H	H-O/O-H	H-C/C-H
ABQ17	H-H: 40.7 %	H-O / O-H: 25.7 %	H-C / C-H: 14.8 %
AQ9	H-H: 58.6 %	H-O / O-H: 17 %	H-C / C-H: 17 %
AQ11	H-H: 38.9 %	H-O / O-H: 14.2 %	H-C / C-H: 20.7 %
AQ17	H-H: 54 %	H-O / O-H: 13.3 %	H-C / C-H: 14.8 %
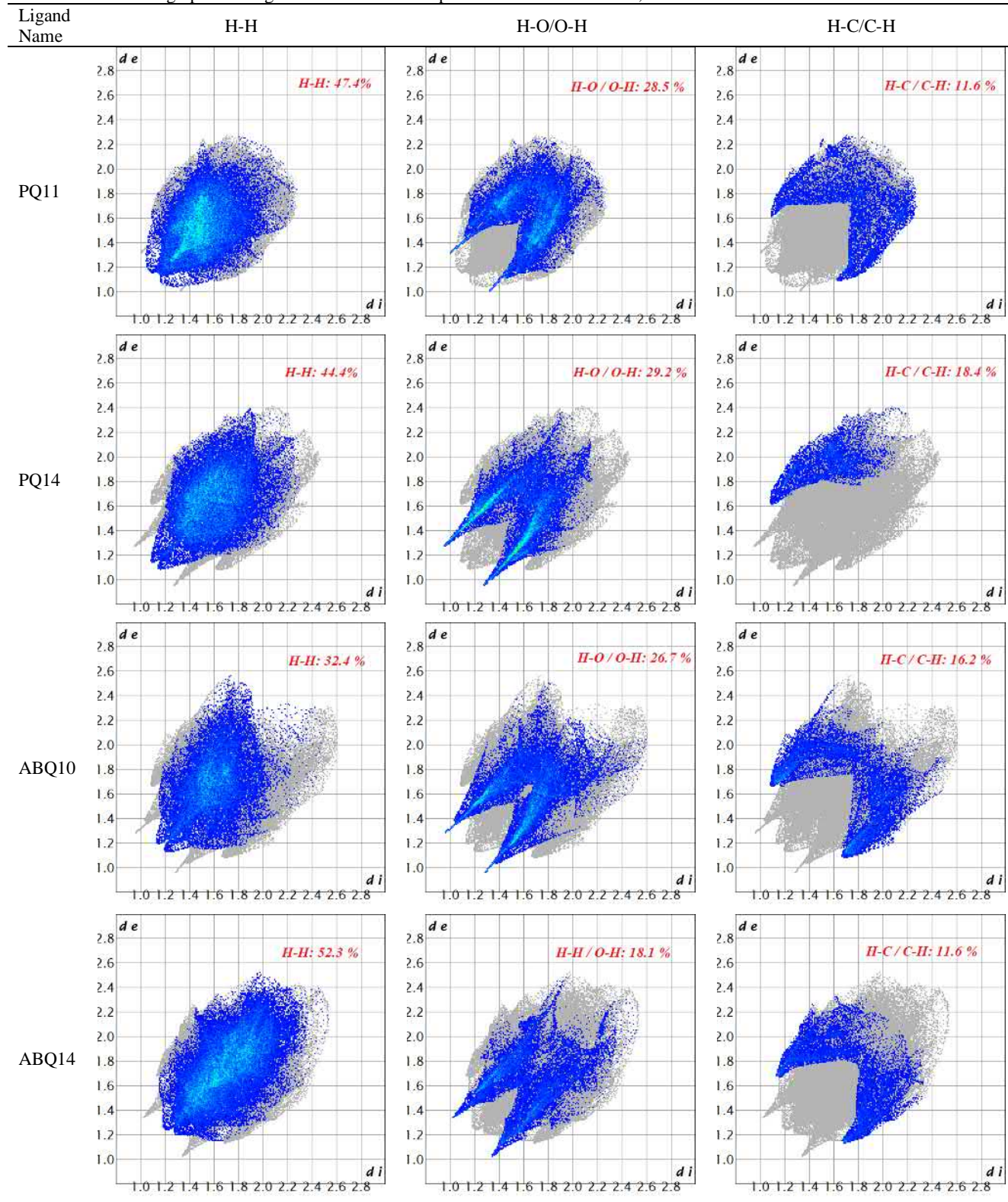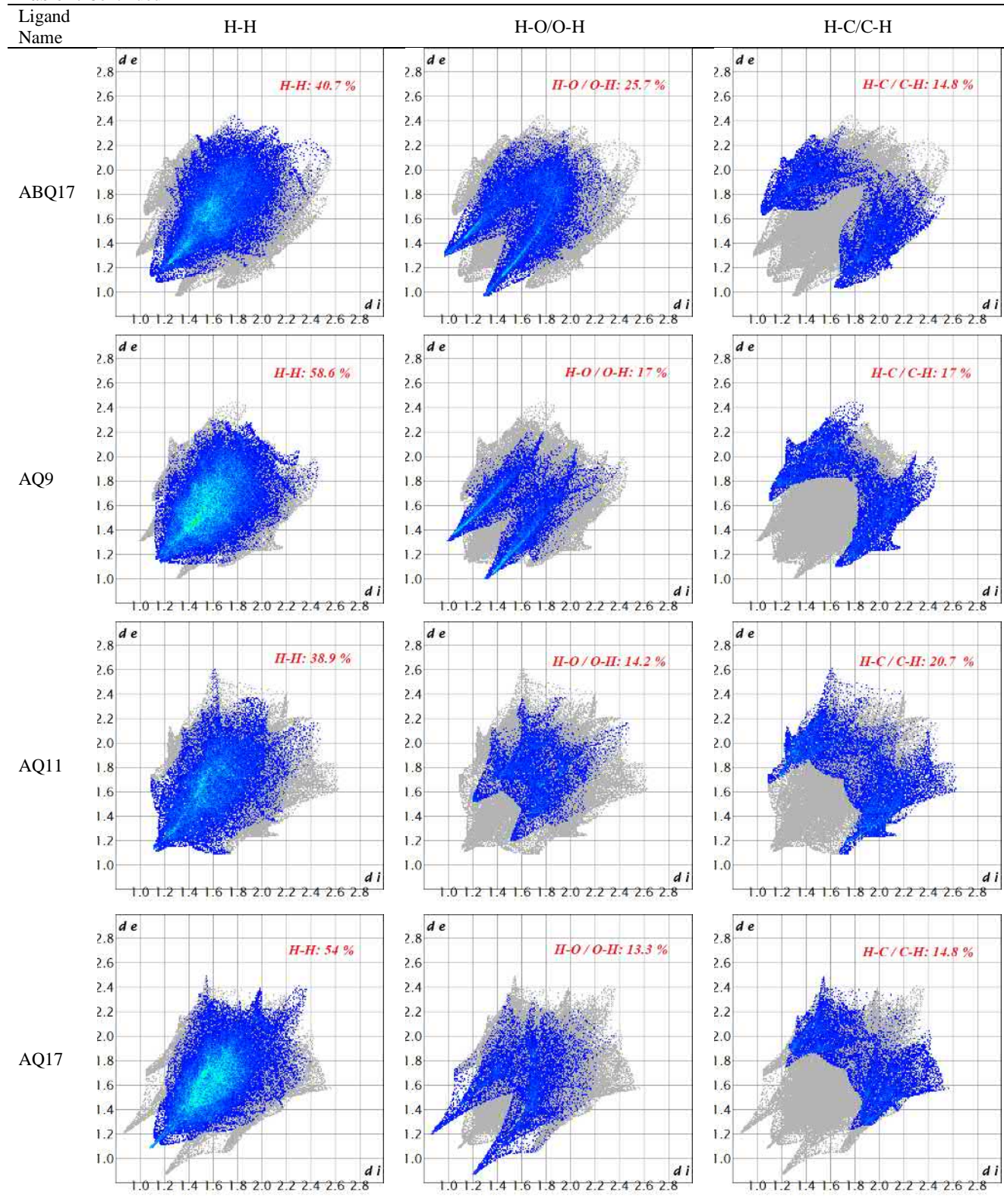
Table 8. The HOMO&LUMO energy and computed other parameters

Parameters	Formula	ABQ16	AQ2	AQ6	ABQ11
LUMO energy (eV)	E_{LUMO}	-3.038	-3.059	-2.903	-3.032
HOMO energy (eV)	E_{HOMO}	-5.475	-6.043	-5.652	-5.266
Energy band gap	$\Delta E = E_{LUMO} - E_{HOMO}$	2.437	2.984	2.749	2.234
Ionization potential	$I = -E_{HOMO}$	5.475	6.043	5.652	5.266
Electron affinity	$A = -E_{LUMO}$	3.038	3.059	2.903	3.032
Chemical hardness	$\eta = (I - A)/2$	1.219	1.492	1.375	1.117
Chemical softness	$\xi = 1/2\eta$	0.410	0.335	0.364	0.448
Electronegativity	$\chi = (I + A)/2$	4.257	4.551	4.278	4.149
Chemical potential	$\mu = -(I + A)/2$	-4.257	-4.551	-4.278	-4.149
Electrophilicity index	$\psi = \mu^2/2\eta$	7.434	6.941	6.656	7.706

Table 9. Mulliken atomic charges

| ABQ16		AQ2		AQ6		ABQ11	
Atom	Charge	Atom	Charge	Atom	Charge	Atom	Charge
C (1)	0,4216	C (1)	0,3925	C (1)	0,3916	C (1)	0,4220
C (2)	-0,2350	C (2)	-0,1898	C (2)	-0,1926	C (2)	-0,2376
C (3)	0,3183	C (3)	0,3159	C (3)	0,3144	C (3)	0,3197
C (4)	0,3747	C (4)	0,3708	C (4)	0,3708	C (4)	0,3742
C (5)	0,0276	C (5)	0,0213	C (5)	0,0208	C (5)	0,0269
C (6)	0,0233	C (6)	0,0374	C (6)	0,0372	C (6)	0,0231
C (7)	-0,3588	C (8)	-0,3603	C (8)	-0,3596	C (7)	-0,3585
C (11)	-0,3607	C (12)	-0,3925	C (12)	-0,3925	C (11)	-0,3616
O (15)	-0,4911	O (16)	-0,4861	O (16)	-0,4968	O (15)	-0,4859
O (16)	-0,4669	O (17)	-0,4923	O (17)	-0,4983	O (16)	-0,4693
N (17)	-0,6775	N (18)	-0,7146	N (18)	-0,6874	N (17)	-0,6746
C (18)	-0,1435	C (19)	-0,0905	C (19)	-0,1362	C (18)	0,3432
C (19)	0,3188	C (20)	-0,0850	C (20)	0,1280	C (19)	-0,1251
C (20)	0,3200	C (21)	-0,1198	C (21)	-0,1241	C (20)	-0,1352
C (21)	-0,1669	C (22)	-0,0733	C (22)	-0,1185	C (21)	0,3282
C (22)	0,2831	C (23)	0,3125	C (23)	0,3144	C (22)	0,2590
C (23)	-0,0794	C (24)	-0,1006	C (24)	-0,0983	C (23)	-0,1355
Cl (28)	0,0246	C (30)	0,8162	C (29)	-0,3819	Cl (26)	0,0220
O (29)	-0,5322	F (31)	-0,2642	H (7)	0,1062	O (27)	-0,5427
O (30)	-0,5297	F (32)	-0,2749	H (9)	0,1363	C (28)	-0,0798
C (31)	0,0275	F (33)	-0,2601	H (10)	0,1106	O (33)	-0,5262
C (32)	0,0289	H (7)	0,1096	H (11)	0,1351	C (34)	-0,0834
H (8)	0,1393	H (9)	0,1396	H (13)	0,1272	H (8)	0,1399
H (9)	0,1112	H (10)	0,1115	H (14)	0,1275	H (9)	0,1105
H (10)	0,1368	H (11)	0,1369	H (15)	0,1538	H (10)	0,1365
H (12)	0,1078	H (13)	0,1284	H (25)	0,0862	H (12)	0,1087
H (13)	0,1457	H (14)	0,1296	H (26)	0,0844	H (13)	0,1446
H (14)	0,1457	H (15)	0,1537	H (27)	0,1060	H (14)	0,1454
H (24)	0,1046	H (25)	0,1034	H (28)	0,2844	H (24)	0,1057
H (25)	0,1038	H (26)	0,0992	H (30)	0,1291	H (25)	0,2993
H (26)	0,2918	H (27)	0,1155	H (31)	0,1165	H (29)	0,1165
H (27)	0,1030	H (28)	0,1163	H (32)	0,1154	H (30)	0,1288
H (33)	0,1190	H (29)	0,2941	H (33)	0,0903	H (31)	0,1149
H (34)	0,1212					H (32)	0,0916
H (35)	0,1244					H (35)	0,1257
H (36)	0,1188					H (36)	0,1238
						H (37)	0,1089
						H (38)	0,0962

Table 10. Mulliken atomic charges with color index and atom numbering (second column), and plotted charge values of each separate atom
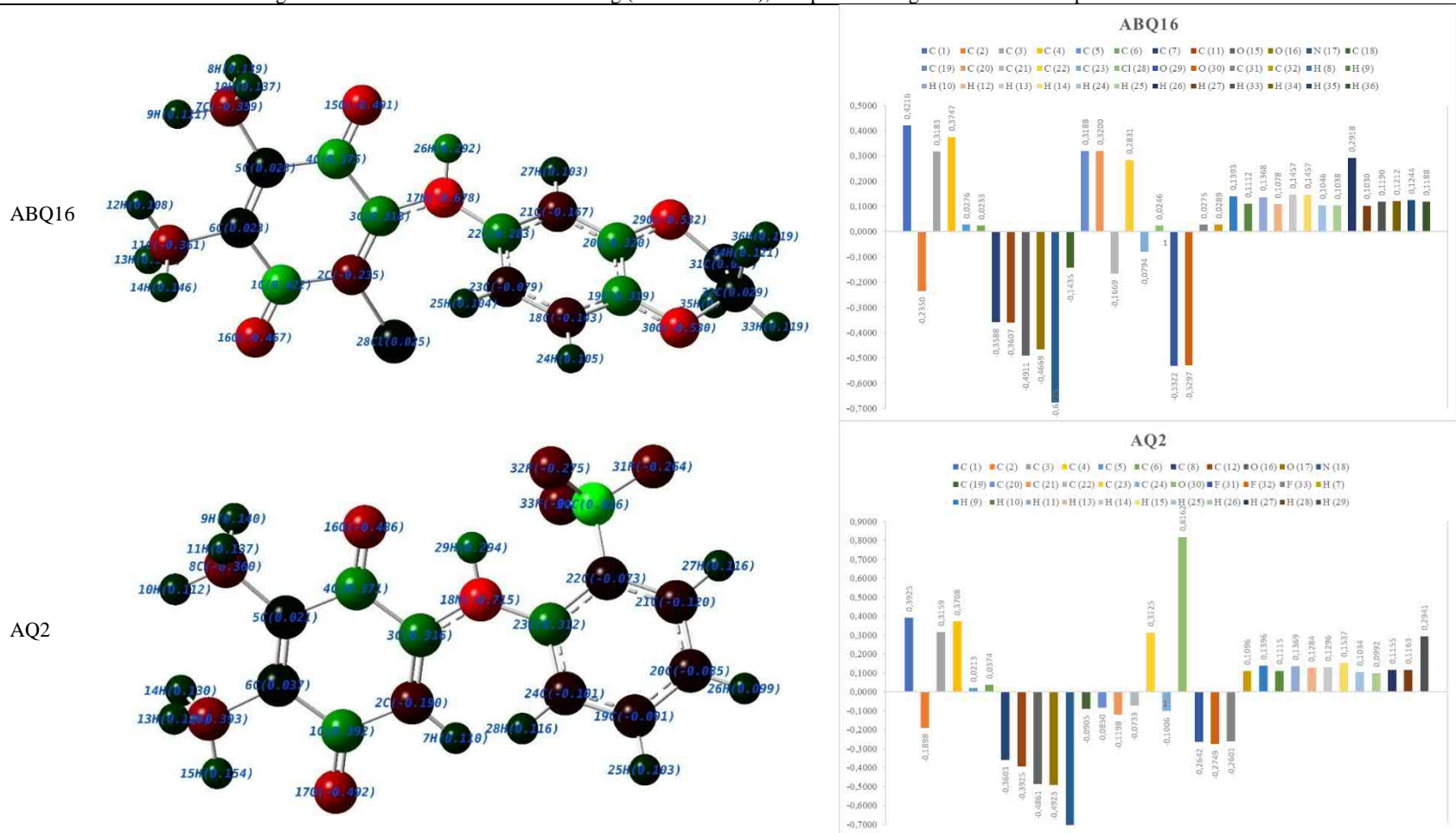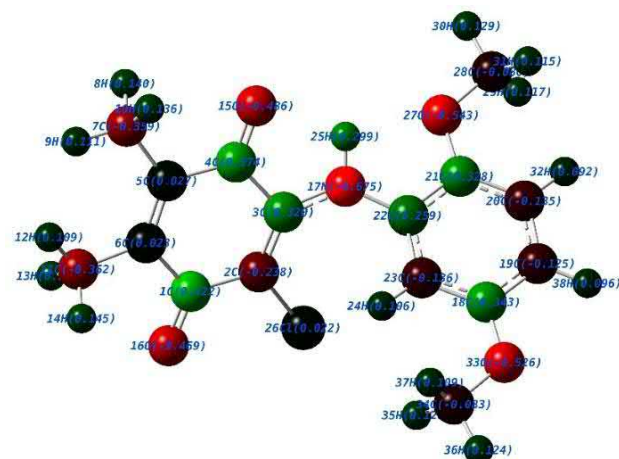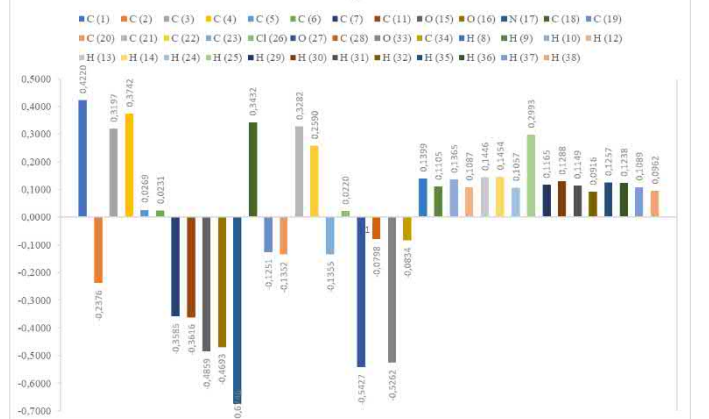
Table 10. Continued
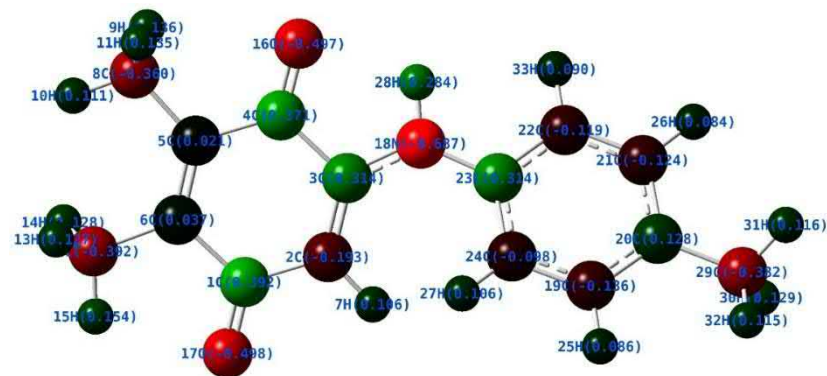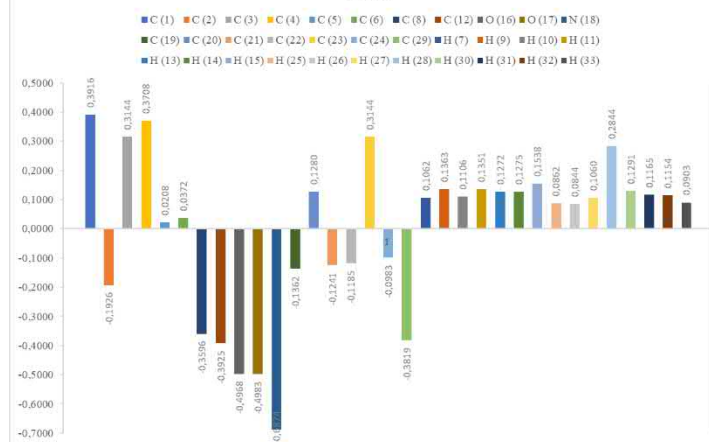
AQ6		
ABQ11		

On Roman Domination in Middle and Splitting Graphs

Betül ATAY ATAKUL[1*]

[1] *Department of Computer Education and Instructional Technology, Ağrı İbrahim Çeçen University,04100, Ağrı, Turkey,*

batay@agri.edu.tr (ORCID: 0000-0003-1964-3287)

Abstract

For a graph $G = (V, E)$, a Roman dominating function(RDF) is a function $f: V \to \{0,1,2\}$ having the property that every vertex u for which $f(u) = 0$ is adjacent to at least one vertex v for which $f(v) = 2$. The weight of an RDF $((w(f))$ is the sum of assignments for all vertices. The minimum weight of an Roman dominating function on graph G is the Roman domination number, denoted by $\gamma_R(G)$. In this paper, we study on this variant of the domination number for middle and splitting graphs of some special graphs.

Keywords: Graph vulnerability, domination, Roman domination.

1. Introduction

Let G be a simple and undirected graph with sets of vertex $V(G)$ and edge $E(G)$. For any vertex $v \in V(G)$, the *open neighbourhood* of v is $N(v) = \{u \in V(G): uv \in E(G)\}$ and *closed neighbourhood* of v is $N[v] = N(v) \cup \{v\}$. The *distance* $d(u,v)$ between two vertices u and v in G is the length of a shortest path between them. The *diameter* of G, denoted by $diam(G)$ is the largest distance between two vertices in $V(G)$. The *eccentricity* of a vertex u, written as $\epsilon(u)$, the maximum value of all $d(u,v)$ values.

The *radius* of a graph G, written as $rad\ G$, the minimum value of all $\epsilon(u)$ values [West 2001]. *The number of the neighbour vertices of the vertex v is called *degree* of v and denoted by $deg_G(v)$, the minimum degree is denoted by $\delta = \delta(G)$ and the maximum degree is denoted by $\Delta = \Delta(G)$.

A vertex cover of a graph G is a set $Q \subseteq V(G)$ that contains at least one endpoint of every edge. The vertices in Q cover $E(G)$ [West 2001]. A vertex v is said to be pendant vertex if $deg_G(v) = 1$. A vertex u is called support if u is adjacent to a pendant vertex [Harary 1969]. A vertex of degree zero is called an isolated vertex. The largest integer not greater than x is denoted by $\lfloor x \rfloor$ and the least integer not less than x is denoted by $\lceil x \rceil$. Let $v \in S \subseteq V$. A vertex u is called a *private neighbour* of v with respect to S (denoted by u is an $S - pn$ of v) if $u \in N[v] - N[S - \{v\}]$. An $S - pn$ of v is external if it is a vertex of $V - S$. The set $pn(v, S) = N[v] - N[S - \{v\}]$ of all $S - pn's$ of v is called the *private neighbourhood set of v* with respect to S. The set S is said to be *irredundant* if for every $v \in S, pn(v, S) \neq \emptyset$ [Cockayne et al. 2004].

The graph with n vertices labeled $x_1, x_2, \ldots, x_n$ and the edges $x_1x_2, x_2x_3, \ldots, x_{n-1}x_n$ is called a path of length $n - 1$, denoted by P_n. The cycle of length n, C_n is the graph with n vertices $x_1, x_2, \ldots, x_n$ and the edges $x_1x_2, x_2x_3, \ldots, x_nx_1$ [Hartsfield and Ringel 1990]. Paths are trees. A tree is a path if and only if its maximum degree is 2. The wheel with $n + 1$ vertices, $W_{1,n}$, is the graph that consists of an $n - cycle$ and one additional vertex that is adjacent to all the vertices of the cycle. The complete graph K_n is the graph with n vertices and every vertex is adjacent to every other vertex [Hartsfield and Ringel 1990]. A star is a tree consisting of one vertex adjacent to all the others. The $n + 1 -$vertex star is the biclique $S_{1,n}$ [West 2001]. The complement $\bar{G}$ of a simple graph G is the simple graph with vertex set $V(G)$ defined by $uv \in E(\overline{G})$ if

and only if $uv \notin E(G)$. A complementary prism of G, denoted by $G\bar{G}$, is the graph obtained by taking a copy of G and a copy of its complement $\bar{G}$ and then joining corresponding vertices by an edge. For arbitrary graphs G and H, we define the *Cartesian product* of G and H to be the graph GxH with vertices $\{(u,v)|u \in G, v \in H\}$. Two vertices (u_1, v_1) and (u_2, v_2) are adjacent in GxH if and only if one of the following conditions is true: $u_1 = u_2$ and v_1 is adjacent to v_2 in H; or $v_1 = v_2$ and u_1 is adjacent to u_2 in G. If $G = P_m$ and $H = P_n$, then the Cartesian product GxH is called the *mxn grid graph* is denoted $G_{m,n}$.

The domination in graph theory has an important role in many fields of study such as optimization, design and analysis of communication networks, social sciences and military surveillance. A *dominating set* in a graph G is a set of vertices of G such that every vertex in $V(G) - S$ is adjacent to at least one vertex in S. The domination number of G, denoted by $\gamma(G)$, is the minimum cardinality of a dominating set of G [Haynes et all. 1998].

Roman domination is a variant of the domination and was introduced by Cockayne et al. in 2004 [Cockayne et al.2004]. A *Roman dominating function* on a graph $G = (V, E)$ is a function $f: V \rightarrow \{0,1,2\}$ satisfying the condition that every vertex u for which $f(u) = 0$ is adjacent to at least one vertex v for which $f(v) = 2$. The idea is that colours 1 and 2 represent either one or two Roman legions stationed at a given location (vertex v). A nearby location (an adjacent vertex (u) is considered to be *unsecured* if no legions are stationed there (i.e. $f(u) = 0$). An unsecured location (u) can be secured by sending a legion to u from an adjacent location (v). But Emperor Constantine the Great, in the fourth century A.D., decreed that a legion cannot be sent from a location v if doing so leaves that location unsecured (i.e. if $f(v) = 1$). Thus, two legions must be stationed at a location ($f(v) = 2$) before one of the legions can be sent to an adjacent location. Thus, Roman domination appears to be a new variety of both historical and mathematical interest [Stewart 1999]. A function $f = (V_0, V_1, V_2)$ is a *Roman dominating function (RDF)* if $V_2 \succ V_0$, where $\succ$ means that the set V_2 dominates the set V_0, i.e. $V_0 \subseteq N[V_2]$. For a graph $G = (V, E)$, let $f: V \rightarrow \{0,1,2\}$ and let (V_0, V_1, V_2) be the ordered partition of V induced by f, where $V_i = \{v \in V| \in f(v) = i\}$ and $|V_i| = n_i$, for $i = 0,1,2$. Note that there exists a 1-1 correspondence

between the functions $f: V \rightarrow \{0,1,2\}$ and the ordered partitions (V_0, V_1, V_2) of V. Thus, we will write $f = (V_0, V_1, V_2)$. The weight of f is $w_f = f(V) = \sum_{v \in V} f(v) = 2n_2 + n_1$. The minimum weight of w_f for every Roman dominating function f on G is called Roman domination number of G. We denote this number with $\gamma_R(G)$. A Roman dominating function of G with weight $\gamma_R(G)$ is called a γ_R −function of G [Cockayne et al.2004, Mojdeh et al. 2019].

A graph G is a *Roman graph* if $\gamma_R(G) = 2\gamma(G)$. Graphs of the form $G = K_1 + H$, where $\gamma(G) = 1$ and $\gamma_R(G) = 2$ are Roman graphs. Equivalently, any graph G of order n having a vertex of degree $n - 1$ is a Roman graph. Complete bipartite graphs are Roman, i.e. $K_{m,n}$ where $\min\{m,n\} \neq 2$, in which case either $\gamma(G) = 1$ and $\gamma_R(G) = 2$, or $\gamma(G) = 2$ and $\gamma_R(G) = 4$. A graph G is Roman if and only if it has a γ_R − $function$ $f = (V_0, V_1, V_2)$ with $n_1 = |V_1| = 0$.

The following figure shows the $f(v)$ values for each vertex $v \in V(G)$. Since $w(f) = \sum_{v \in V} f(v) = 2n_2 + n_1$, we have $\gamma_R(G) = 3$.
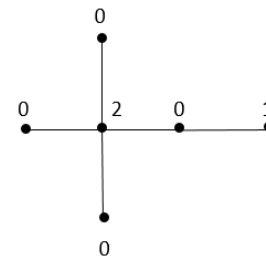
Figure 1.1. The graph G

To date, many articles have been published on the topic of domination as total domination, strong weak domination [Aytaç and Turacı 2015] , exponential domination, semitotal domination [Kartal and Aytaç 2020] etc. and Roman domination. Cockayne et al. introduced the properties of Roman dominating functions. Blidia et al (2020), Chambers et al. (2009), Liu and Chang (2012) researched the bounds on Roman dominating functions and Bermudo et al. (2014) and Xing et al. (2006) discovered the relationships with some domination parameters. Cockayne et al. introduced a linear-time algorithm for computing Roman domination problem on trees [Cockayne et al.2004]. Shirkol et al. (2121) researched the middle Roman domination number of path, cycle, star, double star, wheel, friendship and corona graph. Kazemi (2012) studied on Roman domination for Mycieleski's structure. McRae showed that the

decision problem corresponding to Roman dominating functions (DECIDE-RDF) was NP-complete for bipartite graphs, split graphs and planar graphs. Liedloff et al. (2008) discovered that there were linear-time algorithms for computing the Roman domination number on cographs and interval graphs.

In this paper, our aim is to present the Roman domination number of middle and splitting graphs for $P_n, C_n, S_{1,n}, W_{1,n}$ and K_n. With this work, we have knowledge about the Roman domination number of some special graphs. These results can later be used in larger structures that are their combination. This paper is organized as follows: Section 2 is devoted to some known results about the Roman domination number. Sections 3 and 4 are about the Roman domination number of Middle and Splitting graphs, respectively.

2. Known Results

Theorem 2.1. [Cockayne et al. 2004] For any graph G, $\gamma(G) \leq \gamma_R(G) \leq 2\gamma(G)$.

Proof. Let $f = (V_0, V_1, V_2)$ be a γ_R −function, and let S be a $\gamma - set$ of G. Then, $V_1 \cup V_2$ is a dominating set of G and $(\emptyset, \emptyset, S)$ is a Roman dominating function. Hence, $\gamma(G) \leq |V_1| + |V_2| \leq |V_1| + 2|V_2| = \gamma_R(G)$. But, $\gamma_R(G) \leq 2|S| = 2\gamma(G)$.

Theorem 2.2. [Cockayne et al. 2004] For any graph G of order n, $\gamma(G) = \gamma_R(G)$ if and only if $G = \overline{K_n}$.

Proof. Let $f = (V_0, V_1, V_2)$ be a γ_R −function. The equality $\gamma(G) = \gamma_R(G)$ implies that we have equality in $\gamma(G) \leq |V_1| + |V_2| = |V_1| + 2|V_2| = \gamma_R(G)$. Hence, $|V_2| = 0$, which implies that $V_0 = \emptyset$. Therefore, $\gamma_R(G) = |V_1| = |V| = n$. This implies that $\gamma(G) = n$, which, in turn, implies that $G = \overline{K_n}$.

Theorem 2.3. [Cockayne et al.2004] Let $f = (V_0, V_1, V_2)$ be a γ_R −function. Then

(a) $G[V_1]$, the subgraph induced by V_1 has maximum degree 1.
(b) No edge of G joins V_1 and V_2.
(c) Each vertex of V_0 is adjacent to at most two vertices of V_1.
(d) V_2 is a $\gamma - set$ of $G[V_0 \cup V_2]$.
(e) Let $H = G[V_0 \cup V_2]$. Then each vertex $v \in V_2$ has at least two *H-pn's (*i.e. private neighbours relative to V_2 in the graph $H)$.
(f) If v is isolated in $G[V_2]$ and has precisely one external *H-pn,* say $w \epsilon V_0$, then $N(w) \cap V_1 = \emptyset$.

(g) Let k_1 equal the number of non-isolated vertices in $G[V_2]$, let $C = \{v \in V_0 : |N(v) \cap V_2| \geq 2\}$, and let $|C| = c$. Then $n_0 \geq n_2 + k_1 + c$.

Theorem 2.4. [Cockayne et al. 2004] Let $f = (V_0, V_1, V_2)$ be a γ_R-function of an isolate-free graph G, such that n_1 is a minimum. Then,

(a) V_1 is independent and $V_0 \cup V_2$ is a vertex cover.
(b) $V_0 \succ V_1$.
(c) Each vertex of V_0 is adjacent to at most one vertex of V_1, i.e. V_1 is a 2-packing.
(d) Let $v \in G[V_2]$ have exactly two external *H-pn's* w_1 and w_2 in V_0. Then there do not exist vertices $y_1, y_2 \in V_1$ such that (y_1, w_1, v, w_2, y_2) is the vertex sequence of a path P_5.
(e) $n_0 \geq 3n/7$ and this bound is sharp even for trees.

Theorem 2.5. [Mojdeh et al. 2019] If G is a connected graph of order n, then $\gamma_R(G) \leq \frac{4n}{5}$.

Theorem 2.6. [Mojdeh et al. 2019] For any graph G of order n, we have $\gamma_R(G\bar{G}) \leq n + \gamma(G)$.

Theorem 2.7. [Mojdeh et al. 2019] If G is a graph with no isolated vertices, then $\gamma_R(G\bar{G}) \leq \frac{3n}{2}$.

Theorem 2.8. [Cockayne et al. 2004] For any graph G of order n and maximum degree Δ, $\frac{2n}{\Delta+1} \leq \gamma_R(G)$.

Theorem 2.9. [Cockayne et al. 2004] For a graph G on n vertices, $\gamma_R(G) \leq n\frac{2+\ln((1+\delta(G)/2)}{1+\delta(G)}$.

Theorem 2.10. [Cockayne et al. 2004] For the classes of paths P_n and cycles C_n, $\gamma_R(P_n) = \gamma_R(C_n) = \left\lceil \frac{2n}{3} \right\rceil$.

Theorem 2.11. [Cockayne et al. 2004] Let $G = K_{m_1,\ldots,m_n}$ be the complete *n-partite* graph with $m_1 \leq m_2 \leq \cdots \leq m_n$.

(a) If $m_1 \geq 3$ then $\gamma_R(G) = 4$.
(b) If $m_1 = 2$ then $\gamma_R(G) = 3$.
(c) If $m_1 = 1$ then $\gamma_R(G) = 2$.

Theorem 2.12. [Cockayne et al. 2004] If G is a graph of order n which contains a vertex of degree $n - 1$, then $\gamma(G) = 1$ and $\gamma_R(G) = 2$.

Theorem 2.13. [Cockayne et al. 2004] For the 2 x n grid graph $G_{2,n}$, $\gamma_R(G_{2,n}) = n + 1$.

Theorem 2.14. [Cockayne et al. 2004] If G is any isolate-free graph of order n, then $\gamma_R(G) = n$ if and only if n is even and $G = \left(\frac{n}{2}\right)K_2$.

Theorem 2.15. [Cockayne et al. 2004] If G is a connected graph of order n, then $\gamma_R(G) = \gamma(G) + 1$ if and only if there is a vertex $v \epsilon V$ of degree $n - \gamma(G)$.

Theorem 2.16. [Cockayne et al. 2004] If T is a tree on two or more vertices, then $\gamma_R(T) = \gamma(T) + 1$ if and only if T is a wounded spider.

Theorem 2.17. [Cockayne et al. 2004] If G is a connected graph of order n, then $\gamma_R(G) = \gamma(G) + 2$ if and only if:

    (a) G does not have a vertex of degree $n - \gamma(G)$.

    (b) either G has a vertex of degree $n - \gamma(G) - 1$ or G has two vertices v and w such that $|N[v] \cup N[w]| = n - \gamma(G) + 2$.

Theorem 2.18. [Cockayne et al. 2004] If G is a connected graph and $\gamma_R(G) = \gamma(G) + 2$, then $2 \leq rad(G) \leq 4$ and $3 \leq diam(G) \leq 8$.

Theorem 2.19. [Cockayne et al. 2004] If T is a tree of order $n \geq 2$, then $\gamma_R(G) = \gamma(G) + 2$ if and only if either (i) T is a healthy spider or (ii) T is a pair of wounded spiders T_1 and T_2, with a single edge joining $v \in V(T_1)$ and $w \in V(T_2)$, subject to the following conditions:

    (1) if either tree is a P_2, then neither vertex in P_2 are joined to the head vertex of the other tree.

    (2) v and w are not both foot vertices.

3. Roman Domination for Middle Graphs

In this section, we gived some results about the Roman domination number of middle graphs for path graph P_n, cycle graph C_n, star graph $S_{1,n}$, wheel graph $W_{1,n}$ and complete graph K_n.

Definition 3.1. [Ramakrishnan 1988] The middle graph $M(G)$ of a graph G is the graph whose vertex set is $V(G) \cup E(G)$, and two vertices of $M(G)$ are adjacent if either they are adjacent edges of G or one is a vertex and the other is an edge of G, incident with it.

The star graph $S_{1,4}$ and the middle graph $M(S_{1,4})$ can be depicted as in the following figures:
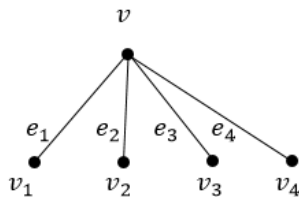
Figure 3.1. Star graph $S_{1,4}$
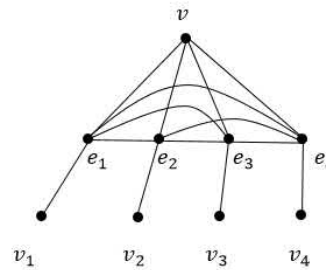
Figure 3.2. Middle graph $M(S_{1,4})$

Theorem 3.1. [Shirkol et al. 2121] Let $M(P_n)$ be a middle graph of the path graph of order $2n - 1$ for $n \geq 2$. Then,

$$\gamma_R\big(M(P_n)\big) = n + 1.$$

Theorem 3.2. [Shirkol et al. 2121] Let $M(C_n)$ be a middle graph of the cycle graph of order $2n$. Then,

$$\gamma_R(M(C_n) = n.$$

Theorem 3.3. [Shirkol et al. 2121] Let $M(W_{1,n})$ be a middle graph of the wheel graph of order $3n + 1$. Then,

$$\gamma_R(M\big(W_{1,n}\big) = n - 1.$$

Theorem 3.4. [Shirkol et al. 2121] Let $M(S_{1,n})$ be a middle graph of the star graph of order $2n + 1$. Then,

$$\gamma_R(M\big(S_{1,n}\big) = n + 1.$$

Proof. The vertex v and vertices $e_1, e_2, \dots, e_n$ are make up the complete graph K_{n+1}. We know $\gamma_R(K_n) = 2$. Since the remaining vertices $v_1, v_2, \dots, v_n$ are independent, $V_2 > V_0$ and V_1 and V_2 have no edges between them, $e_i \in V_2$, where each i is related to exactly one $1, 2, \dots, n$. So, $|V_2| = 1$ and $v_i \in V_0$ $i = \overline{1,n}$ due to $d(v_i, e_i) = 1$. Hence, $|V_1| = n - 1$ and we have $\gamma_R(M\big(S_{1,n}\big) = f(V) = \sum_{v \in V} f(v) = 2n_2 + n_1 = 2 + n - 1 = n + 1$.

Theorem 3.5. Let $M(K_n)$ be a middle graph of the complete graph of order $n + \binom{n}{2}$. Then,

$$\gamma_R(M(K_n)) = n.$$

Proof. We can split the vertex set of the $M(K_n)$ as $V(M(P_n) = V\big(V(K_n)\big) \cup V(E(K_n)), v_i \in V(K_n), i = \overline{1,n}$ and $e_{i,j} \in V\big(E(K_n)\big), i = \overline{1, n-1}, j = \overline{i+1, n}$. $\big|V\big(V(K_n)\big)\big| = n$ and $|V(E(K_n))| = \binom{n}{2}$. Also, $\deg\big(e_{i,j}\big) = 2n - 4$ for $\forall e_{i,j} \in V(E(K_n))$ and $\deg(v_i) = n - 1$ for $\forall v_i \in V(K_n)$. Let $f = (V_0, V_1, V_2)$ be a $\gamma_R - function$ and S be a $\gamma - set$ of $M(K_n)$. Then, $V_1 \cup V_2$ is a dominating set of $M(K_n)$

and $(\emptyset, \emptyset, S)$ is a Roman dominating function. We have two cases:

Case 1. $n \equiv 0 \pmod 2$

In this case, $\frac{n}{2}$ vertices $e_{i,i+1}, i = 1,3,5,\dots,n-1$ make up V_2. So, all vertices are dominated. $\gamma_R(M(K_n)) = 2\gamma(M(K_n))$. $f(V) = \sum_{v \in V} f(v) = 2n_2 + n_1 = 2\left(\frac{n}{2}\right) = n$.

Case 2. $n \equiv 1 \pmod 2$

In this case, $\left\lfloor \frac{n}{2} \right\rfloor$ vertices $e_{i,i+1}, i = 1,3,5,\dots,n-2$ make up V_2. So, $\forall e_{i,j}$ and $v_1, v_2, \dots, v_{n-1}$ are dominated. The vertex v_n make up V_1. Hence, $f(V) = \sum_{v \in V} f(v) = 2n_2 + n_1 = 2\left\lfloor \frac{n}{2} \right\rfloor + 1 = n$.

So, we have $\gamma_R(M(K_n) = n$ from Case 1 and Case 2.

4. Roman Domination for Splitting Graphs

In this section, we investigated the Roman domination number of splitting graphs for path graph P_n, cycle graph C_n, star graph $S_{1,n}$, wheel graph $W_{1,n}$ and complete graph K_n.

Definition 4.1.[Sampathkumar, E. and Walikar 1980] *Splitting graph* $S(G)$ of a graph G is obtained by taking a copy of G, for each vertex v of a graph G, take a new vertex v' and join v' to all the vertices of G adjacent to v.

The path graph P_5 and the splitting graph $S(P_5)$ can be depicted as in the following figures:
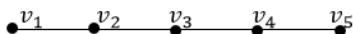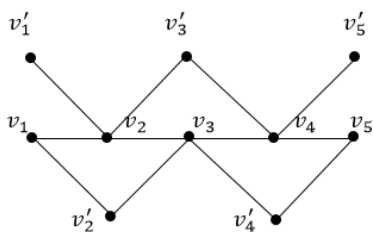

Figure 4.1. Path graph P_5

Figure 4.2. Splitting graph $S(P_5)$

Theorem 4.1. Let $S(P_n)$ be a splitting graph of the path graph of order $2n$. Then,

$$\gamma_R(S(P_n)) = \begin{cases} n, & n \equiv 0 \pmod 3 \\ n+1, & n \equiv 1,2 \pmod 3 \end{cases}$$

Proof. Let $f = (V_0, V_1, V_2)$ be the RDF of $S(P_n)$. The value of the function for the corresponding vertices v_i'

, $i = \overline{1,n}$ is $f(v_i') = 0$ if $f(v_i) = 0$; $f(v_i') = 1$ if $f(v_i) = 1$ or $f(v_i) = 2$, respectively. We know $\gamma_R(P_n) = \left\lceil \frac{2n}{3} \right\rceil$ from the Theorem 1.9. So, we have three cases:

Case 1. $n \equiv 0 \pmod 3$

In this case, $f(v_i) = 0, f(v_{i+1}) = 2, f(v_{i+2}) = 0$ and $f(v_i') = 0, f(v_{i+1}') = 1, f(v_{i+2}') = 0$ for $i = 1,4,7,\dots,n-2$. Hence, $f(V) = \sum_{v \in V} f(v) = 2n_2 + n_1 = \frac{2n}{3} + \frac{n}{3} = n$.

Case 2. $n \equiv 1 \pmod 3$

In this case, $f(v_i) = 0, f(v_{i+1}) = 2, f(v_{i+2}) = 0$ and $f(v_i') = 0, f(v_{i+1}') = 1, f(v_{i+2}') = 0$ for $i = 1,4,7,\dots,n-3$. Also, $f(v_n) = f(v_n') = 1$. Hence, $f(V) = \sum_{v \in V} f(v) = 2n_2 + n_1 = \left\lceil \frac{2n}{3} \right\rceil + \frac{n-1}{3} + 1 = \left\lceil \frac{2n}{3} \right\rceil + \frac{n+2}{3} = n + 1$.

Case 3. $n \equiv 2 \pmod 3$

In this case, $f(v_i) = 0, f(v_{i+1}) = 2, f(v_{i+2}) = 0$ and $f(v_i') = 0, f(v_{i+1}') = 1, f(v_{i+2}') = 0$ for $i = 1,4,7,\dots,n-4$. Also, $f(v_n) = 2$ and $f(v_n') = 1$. Hence, $f(V) = \sum_{v \in V} f(v) = 2n_2 + n_1 = \left\lceil \frac{2n}{3} \right\rceil + \frac{n-2}{3} + 1 = \left\lceil \frac{2n}{3} \right\rceil + \frac{n+1}{3} = n + 1$.

So, from Case 1, Case 2 and Case 3, we have

$$\gamma_R(S(P_n)) = \begin{cases} n, & n \equiv 0 \pmod 3 \\ n+1, & n \equiv 1,2 \pmod 3 \end{cases}$$

Corollary 4.1. Let P_n be a path graph of order n and $S(P_n)$ be a splitting graph of the path graph of order $2n$. Then,

$$\gamma_R(S(P_n)) = \begin{cases} \gamma_R(P_n) + \dfrac{n}{3}, & n \equiv 0 \pmod 3 \\ \gamma_R(P_n) + \dfrac{n+2}{3}, & n \equiv 1 \pmod 3 \\ \gamma_R(P_n) + \dfrac{n+1}{3}, & n \equiv 2 \pmod 3 \end{cases}$$

Theorem 4.2. Let $S(C_n)$ be a splitting graph of the cycle graph of order $2n$. Then,

$$\gamma_R(S(C_n)) = \begin{cases} n, & n \equiv 0 \pmod 3 \\ n+1, & n \equiv 1,2 \pmod 3 \end{cases}$$

Proof. The proof is similar to the proof of the Theorem 4.1.

Theorem 4.3. Let $S(S_{1,n})$ of order $2n + 2$, $S(W_{1,n})$ of order $2n + 2$ be splitting graphs of a star graph and a wheel graph respectively and $S(K_n)$ of order $2n$ be a splitting graph of a complete graph. Then, $\gamma_R\left(S(S_{1,n})\right) = \gamma_R(S_{1,n}) + 1, \gamma_R\left(S(W_{1,n})\right) = \gamma_R(W_{1,n}) + 1$ and $\gamma_R(S(K_n)) = \gamma_R(K_n) + 1$.

Proof. We denote $S_{1,n}$, $W_{1,n}$ and K_n by G. $\exists u \in G|$ $\deg(u) = n$ in G. Let $f = (V_0, V_1, V_2)$ be the RDF of $S(G)$. We denote the corresponding vertices of v_i by $v_i', i = \overline{1,n}$ in $S(G)$. If $f(u) = 2$, then $f(v_i) = f(v_i') = 0$, since $d(u) = d(v_i) = d(v_i') = 1$. So, $\{u'\} = V_1$. We have $\gamma_R(G) = 2\gamma(G)$ and $\gamma_R(S(G)) = \gamma_R(G) + 1$.

Corollary 4.2. Let G be a graph of order n. If $\exists v \in V(G)|\deg(v) = n-1$, then $\gamma_R(S(G)) = \gamma_R(G) + 1$.

References

AYTAÇ, A. and TURACI, T. (2015). Strong Weak Domination in Complementary Prisms, Dynamics of Continuous, Discrete and Impulsive Systems Series B: Applications and Algorithms, 22(2), 85-96.

BERMUDO, S.,FERNAU, H.,SIGARRETTA, J. (2014). The Differential and the Roman Domination Number of a Graph, Appl. Anal. Discret. Math., 8, 155-171.

BLIDIA, M., BOUCHOU, A., CHELLALI, M. (2020). Extremal Graphs for a Bound on the Roman Domination Number, Discuss. Math. Graph Theory, 40, 771-785.

CHAMBERS, E.W., KINNERSLEY, B., PRINCE, N., WEST, D.B. (2009). External Problems for Roman Domination, SIAM j. Discret Mathematics, 23(3) 1575-1586.

COCKAYNE, E.J., DREYER Jr, P.A., HEDETNIEMI, S.A. (2004). Roman Domination in Graphs, Discrete Mathematics, 11-22.

HARARY, F. (1969). Graph Teory, In: Addition-Wesley Publishing Co. Reading, MA/Menlo Park, CA/London.

HARTSFIELD, N. and RINGEL, G. (1990). Pearls in Graph Theory, In: Academic Press, INC.

HAYNES, T.W., HEDETNIEMI, P.J., SLATER, P.J. (1998). Fundamentals of Domination in Graphs, Marcel Dekker, New York.

KARTAL, Z. and AYTAÇ, A. (2010). Semitotal Domination of Harary Graphs, Tbilisi Mathematical Journal, 3, 11-17.

KAZEMI, A.P., (2012). Roman Domination and Mycieleski's structure in Graphs, Ars Combinatoria, 106, 277-287.

LIU, C.H. and CHANG, G.J.(2012). Upper Bounds on Roman Domination numbers of Graphs, Discret. Math., 312, 1386-1391.

LIEDLOFF, M., KLOKS, T., LIU, J., PENG, S.L. (2008). Efficient Algorithms for Roman Domination on Some Classes of Graphs, Discret. Appl. Math., 156, 3400-3415.

MOJDEH, D.A., PARSIAN, A., MASOUMI, I. (2019). Strong Roman Domination Number of Complementary Prism Graphs, Turk. J. Math. Comput. Sci, 40-47.

RAMAKRISHNAN,(1988).MPhil-Thesis, Pondicherry University, Puducherry, India.

SAMPATHKUMAR, E. & WALİKAR, H.B. (1980). On the Splitting Graph of a Graph, The Karnataka University Journal Science, 25&26, 13-16.

SHIRKOL,S.S.,KUMBARGOUDRA,P.P., KALIWAL, M.M, (2021). On Roman Domination in Middle Graphs, Journal of Shanghai Jiaotong University, 17(7), 10-18.

STEWART, I. (1999). Defend the Roman Empire!, Sci. Ame., 281,136-139.

WEST, D.B. (2001). Introduction to Graph Theory, In: Pearson Education (Second Edition)

XING, H.M., CHEN, X., CHEN X.G. (2006). A Note on Roman Domination in Graphs, Discret. Math., 306, 3338-3340.

Investigation of epithermal and fast neutron shielding properties of Some High Entropy Alloys Containing Ti, Hf, Nb, and Zr

Bünyamin Aygün[1]*, Abdulhalik Karabulut[2]

*[1]*Department of Electronics and Automation, Vocational School, Agri Ibrahim Cecen University, Agrı, Turkey*

baygun@agri.edu.tr (ORCID:0000-0002-9384-1540)

[2]Department of Physics, Faculty of Science, Atatürk University, 25040, Erzurum, and Agri Ibrahim Cecen University, Agrı, Turkey

akara@atauni.edu.tr (ORCID:0000-0003-2290-9007)

Abstract

High entropy alloys often have excellent mechanical properties that conventional alloys based on one or two elemental combinations do not have. It is necessary to investigate whether these alloys can be used for nuclear applications with their properties such as high strength, fracture toughness, high corrosion and wear resistance. In this study, the thermal and fast neutron absorption properties of high entropy alloys with three different contents including Ti, Ta, Hf, Nb, and Zr elements were investigated. Their usability for nuclear applications has been demonstrated. In order to understand whether a material is neutron shielding, important neutron attenuation parameters such as effective removal cross section, half value layer, mean free path and neutron transmission factor (NTF) need to be determined. These reduction parameters were theoretically found with the Monte Carlo simulation GEANT4 code for epithermal and fast neutrons. It was found that Nb25 Ti25Hf25Ta25 has the best neutron shielding capacity among the investigated High entropy alloys. According to found all the results in the present work, we suggest that the all high entropy alloy samples can be used against any neutron leaks in nuclear operations.

Keywodrs High entropy alloys, Geant4, Neutron, Shielding

1. Introduction

Radiation is widely used in energy production, medicine, archaeological, military, mining, space exploration, and investigations (WRIXON. 2013). Neutron radiation is widely used in condensed matter physics, crystallography, geology and mineralogy, biology, materials research, solid-state chemistry, and scattering and diffraction experiments. Neutron radiation has been successfully used in the destruction of tumors by at a high rate penetrating cells and tissues. During these processes, staff or patients can stay exposed to radiation. If exposed to high dose neutron, it can be damaged tissue, and cells such as vomiting, skin burns, acute ivegen, and the development of cancer. The best method of protecting against radiation is using quality shielding materials (PARK et al. 2014). Many samples were developed and produced for shielding neutron radiation such as stainless steel (AYGUN 2019a), (AYGUN et al. 2019b), (ALIM et al. 2022), (EID et al. 2022) some metals added alloys (RAMMAH et al. 2021), (EL-AGAWANY et al. 2021), (KORKUT et al. 2015) newly developed consist of metal oxide special glasses (AYGUN, et al. 2020a), (ELSAFI et al. 2021), (YIN et al. 2022) (AYGUN, et al. 2020b) reinforced heavy concretes (SARİYER & KÜÇER 2020), (AYGUN, et al. 2019c), (KINNO et al. 2002), (AYGUN et al. 2018) elastic and nonelastic high-density polymers (BILICI et al. 2021). (AYGUN et al. 2015), (HU et al. 2020).

High entropy alloys are a new type of alloy formed by using element concentrations from 5% to 35%. Incorporation into an alloy at the same mixing ratios in the same proportions ensures the formation of high entropy. High Entropy Alloys have properties such as high temperature, structural stability, strength, superior wear, and good corrosion resistance (MARY et al. 2015). High entropy alloys are excellent materials used in automotive, aerospace, gas turbine engine, exhaust nozzles, combustion chambers, and many similar

applications. Due to their superior properties, these alloys are used as protective materials in nuclear applications like other sectors (PICKERING et al. 2021). Elastic composite materials containing low melting point polydimethylsiloxane and high entropy alloy are made for the radiation shield. GaInSnPbBi high entropy alloy was used as a filler to increase the radiation shielding ability and it was suggested that this alloy could be used for this type of composite structure. linear attenuation coefficient (LAC), tenth value layer (TVL), and effective atomic number (Zeff) were calculated using MCNPX software. It has been suggested that these composites can be used as a shielding material in X-ray applications (WANG et al. 2021). High entropy alloys (HEA) are preferred as a coating material in next-generation nuclear reactors III+ and IV because they have low thermal neutron cross sections and high melting points. HEAs were produced consisting of NbTiVZrx (x = 0.5, 1, 2) chemical formula according to it including Zr varied ratios experimentally and then cross-section calculated (KING et al. 2019). Low activation high entropy alloys (HEAs) with TiVZrTa and TiVCrTa chemical formulas were designed and produced for use as in-core, structural power reactors materials. After exposure to heavy ion implantation, the new alloys were found to have good irradiation resistance (KAREER et al. 2019). New developed TiTaHfNb, TiTaHfNbZr, and TiTaHfMoZr high entropy alloys are used in medical applications because of their superior resistance to corrosion and compatibility with human tissue (GUREL et al. 2021).

When a neutron with an energy of 1 MeV or more interacts with an alloy material, the neutron collides with an atom in the alloy and this atom gains a certain amount of kinetic energy and can be displaced in the molecular lattice region. This primary displacement causes the atoms and other atoms to be displaced by collision, causing the atoms to slide in the lattice. This event, which causes the displacement of a large number of atoms, causes the formation of spatial gap + interstitial Frenkel pairs. This is a primary damage to the material and can be permanent (ZINKLE, 2012). In fact, this movement causes an increasing temperature increase from the inside to the outside in the alloy, resulting in thermal structural deterioration. In the future, a new generation of fusion reactors will be built to ensure energy needs. In these reactors, high flux fast neutrons with 14.1 MeV energy will cause damage above100 dpa because they form hyper temperatures in the reactor components. This situation will cause high corrosion in protective components and can create cracks in the shielding material. Radiation leaks may occur as a result of this may occur at high entropy alloys can be used to prevent these leaks (KING et al. 2017).

In this presented study, the fast neutron radiation shielding parameters have been theoretically calculated for three high entropy alloys Monte Carlo Simulation Geant4 (GEometry ANd Tracking 4) software was used.

2. Theoretical background

A practical, convenient, and appropriate way to determine the severity of neutrons is to obtain the number of neutrons (N/cm²) per unit area (n/cm²) or flow rate (n/cm²s). The flow of neutrons with an intensity I intensity is reduced by the shielding material with the x -thickness of the neutron source depending on the severity of the source and the coefficient of the neutron transmission (σnr). Similar to the Lambert-Beer Law used for the absorption of photons, the following statement for neutrons is valid:

$$I(x) = I_0 e^{-\Sigma_{nr} x} \tag{1}$$

Neutrons can interact with a material such as elastic, inelastic, neutron capture, or fission when colliding with it.

The probabilities of these interactions that neutrons can make with the materials they collide with are expressed by the effective removal cross-section and the total macroscopic cross-section (∑t), and this value can be calculated as follows. (AYGUN 2019 a).

$$\sum t = \sum N(\sigma t) \tag{1}$$

N; represents the number of nuclei per unit volume contained in the target material.

The total microscopic cross-section σt indicates the probability of interaction of neutrons of given energy with lower-density target materials, and this value is determined by the sum of the other scatterings, the microscopic sectional scattering (σs), and the microscopic section attenuation (σa).

$$\sigma_t = \sigma_s + \sigma_a \tag{2}$$

The effective removal cross-section, ∑R (cm2/g), refers to the probability of a fast or fission energy neutron's first collision with the shielding material it encounters. (SINGH & BADIGER 2014). If the neutrons interact with the shielding material in the form of a mixture, the effective removal sections for the mass-to-weight ratio of each element in this mixture can be determined as follows.

$$\sum R = \sum \left(\frac{\sum R}{\rho}\right) i \qquad (3)$$

$\sum$R; is the effective removal cross-section of the shielding material and ρ; stands for density.

Half value layer (HVL) indicates the thickness of the material that halves the neutrons passing through the shielding material, and this value is found as follows.

$$HVL = \frac{ln2}{\sum R} \qquad (4)$$

The mean free path (λ) shows the average distance that neutrons can travel in the target material they enter without first colliding, and this value can be calculated by the equation given to follow.

$$\lambda = 1/\sum R \qquad (5)$$

The number of neutrons that pass through the shielding material with or without any interaction is determined by the Neutron transmission factor (NTF). The fact that this value is small indicates that the shielding material has high stopping power and this can be calculated as follows (SCHOBER, 2014), (SAHADATH et al., 2015).

$$NTF = \frac{I}{I_0} \qquad (6)$$

I is the number of neutrons passing through the target material and I_0 is the number of neutrons coming into the material.

3. Material and Method

Geant4 Monte Carlo simulation technique

GEANT4 (Geometry and Tracing) is a Monte Carlo-based tool kit for predicting the events that particles and photons can generate when interacting with the target material. This kit is used in modern particle, high energy, and nuclear physics application experiments to predict situations where detectors and radiation can occur with target material at the same time. The Geant4 kit offers the opportunity to examine the interaction states of many elements and materials with radiation in a wide range of energy levels from eV to TeV' in hadronic and charged particles, electromagnetic and optical applications (AGOSTINELLI et al., 2003).

When using the program, all elements, molecules, compounds and material contents to be studied are defined in the detector and material interface library. At the start of

the simulation process, this information is transferred to the worksheet. In this study, simulation calculations were performed for neutrons in the energy range of 3-14 MeV, using the GEANT4.10.2 version according to the geometry given in Figure 1.
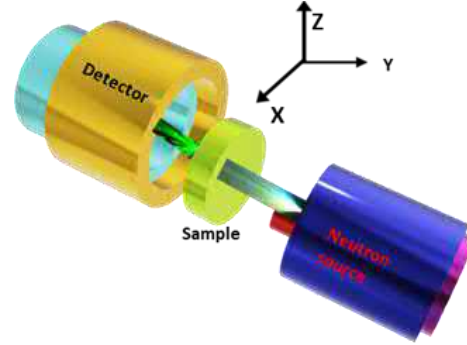
Figure1. Geant4 simulation geometry design

4. Results and Discussion

In this study, the samples (Ti25Ta25Hf25Nb25, Ti20Ta20Hf20Nb20Zr20, Ti20Ta20Hf20Mo20Zr20) whose chemical components are given in Table 1 were used. Some important neutron shielding parameters such as effective removal cross-section (cm $^{-1}$), half value layer (HVL), mean free path (MFP), and neutron transmission factor (NTF) were calculated with Geant4 code.

Neutron radiation attenuation properties

In this study, by using the Geant4 code for the simulation of neutron attenuation parameters such as removal cross-section, MFP, half value layer and transmission number were theoretically calculated with the simulation geometry in Figure 1.

The obtained data were compared with both, 316 LN stainless steel, which has (68.74Fe%+16%Cr+10%Ni+2% Mo+2% Mn+1%Si+0.15%N+0.045%P+0.03%C+ 0.03%S) chemical content and 8g/cm^3 density, and paraffin has ($C_nH_{2n}+_2$) chemical content and 1.2 g/cm^3 density.

The fast neutron attenuation parameters are given in Table 2 and Figure 2. of three types of high entropy alloys for 3-14 MeV energy.

The effective removal cross-section (cm^{-1}) is a useful parameter to consider in neutron shielding studies.

The greater the neutron effective removal cross-section value of a material to be selected as a shielding material, the greater the probability that the neutrons on the material will collide with the atoms of this shielding material. It is a desirable

property for a shielding material to be used for neutrons to have a highly effective removal cross-section.

The fact that this value is large indicates that the shielding material will also have a good absorption power. When Figure 2 is carefully examined, it is seen that the Effective Removal Cross-Section values of all studied samples decrease with increasing neutron energies. Because when the energies of the incoming neutrons increase, the elastic scattering numbers that neutrons can do with the material can also increase, and in this case, the possibility of interacting

with the shielding material decreases. Looking at Figure 2, it is seen that the Effective removal cross-section values of all the samples examined are quite high compared to the paraffin selected as the reference sample, the HEA1 sample is higher than the 316 LN stainless steel and the others have close values. In particular, it was determined that the HEA1 sample had a higher value than all other samples. Considering these results, it is obvious that the shielding capacity of these HEA samples is high against fast neutrons.

Table 1 The chemical component of samples

| Element	HEA1 (ρ=10.64 g/cm^3)	HEA2 (ρ=9.81 g/cm^3)	HEA3 (ρ=10.18 g/cm^3)
Ti	25	20	20
Ta	25	20	20
Hf	25	20	20
Nb	25	20	-
Zr	-	20	20
Mo	-	-	20

HEA (High entropy alloys)

Table 2
Comparison of high entropy alloys fast neutron shielding parameters for 2 cm sample thick and 10^5 incident neutrons

Sample code	Dose Energy (MeV)	Half Value Layer (cm)	Mean Free Path λ (mm)	Neutron Transmission Factor	Effective Removal cross section
P	3	15.098±0.150	21.7±0.212	0.63013	0.459
	6	22.282±0.221	32.1 ±0.312	0.73199	0.311
	9	22.720±0.227	40.0 ±4.157	0.77873	0.250
	12	28.999±0.289	41.8 ±0.286	0.78675	0.239
	14	32.383±0.323	46.7 ±0.480	0.80661	0.214
316LN	3	11.286±0.112	16.25 ±0.180	0.54082	0.614
	6	12.486±0.124	18.01 ±0.182	0.57361	0.555
	9	12.481±0.127	18.06±0.186	0.57402	0.515
	12	14.318±0.143	20.66±0.206	0.61597	0.484
	14	15.503±0.155	22.37±0.223	0.63953	0.447
HEA1	3	10.896±0.108	15.72 ±0.145	0.52898	0.636
	6	12.419±0.124	17.92±0.178	0.57185	0.558
	9	13.430±0.134	19.37±0.192	0.59665	0.516
	12	14.085±0.130	20.32±0.203	0.61098	0.492
	14	14.407±0.144	20.79±0.207	0.61769	0.481
HEA2	3	12.031±0.120	17.36±0.172	0.56160	0.576
	6	13.404±0.134	19.34±0.182	0.59619	0.517
	9	14.114±0.140	20.36±0.205	0.61144	0.491
	12	14.744±0.145	21.27±0.212	0.62478	0.470
	14	15.098±0.150	21.76±0.217	0.63160	0.459

	3	11.627±0.115	16.778±0.162	0.55068	0.596
	6	12.977±0.129	18.726±0.182	0.58579	0.534
HEA3	9	13.695±0.136	19.762±0.195	0.60246	0.506
	12	14.171±0.141	20.449±0.204	0.61317	0.489
	14	14.713±0.145	21.231±0.210	0.62390	0.471

Sample Code: P (Paraffin), **316LN** (Nuclear stainless steel), **HEA** (High entropy alloys)
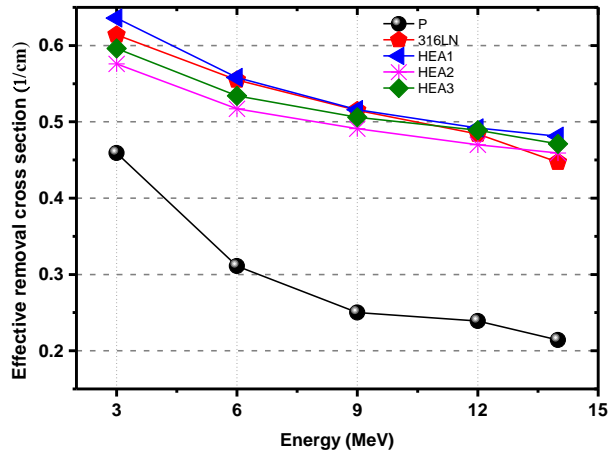
Figure 2. Theoretical 3-14 MeV Neutron Effective Removal Cross Sections

Figure 3. Variation of MFP values for different samples in the energy range of 3- 14 MeV.

A material's low MFP values indicate that it has good neutron-stopping power (TEKIN et al., 2022). Looking at the values in Table 2' and Figure 3; the MFP values of all samples are lower than paraffin. Accordingly, all HEA samples have a greater neutron absorption power than paraffin. All these results showed that the ability of HEA samples to stop neutrons is high. Accordingly, all HEA samples have a greater neutron absorption power than paraffin. Again, while the MFP values of HEA1 sample are lower than 316LN stainless steel, these values of other samples are close. All these results showed that the ability of HEA samples to stop neutrons is high.

Determining the number of neutrons that pass through the target material, which is particle-type radiation, is closely related to the power of that material to stop neutrons. Because the low number of neutrons passing through a material is proof that the material does not allow neutrons to pass through and as a result shows good shielding properties.

The number of neutron particles interacting with the shielding material is closely related to the neutron flux per unit volume. The amount of this flux depends on the probability of elastic, inelastic, scattering, and trapping interactions of neutrons with the shielding material. In other words, the determination of the neutron transition rate can provide information about the absorption capacity of shielding materials (SCHOBER 2014). It is desirable that this value is low.

In this study, transmission rates were determined by sending 10^5 neutrons to the materials. The results found are displayed in Table 2. According to Table 2, the transmission numbers of all HEA samples are lower than paraffin. Accordingly, the materials absorbed more neutrons than paraffin. Likewise, this value of the HEA1 sample is lower than that of 316LN stainless steel, so this sample has a higher rate of neutron suppression than 316LN. Other examples, HEA2 and HEA3,

have values close to 316LN. They showed good stopping performance against neutrons in these samples.

Half value layer (HVL) refers to the material thickness that absorbs half of the neutrons interacting with the shielding material. A material to be used against neutrons should have low HVL values. Because neutrons will travel a long way in materials that are used too thickly, and during this time, they will cause the material to heat up by vibrating the material atoms as a result of their interactions with the atoms of the shielding material. Micro and macro deformations will occur due to thermal expansions in this heated shielding material, and as a result, the probability of neutron leaks will increase. The material half thicknesses, that is, the HVL values, which will halve the amount of neutrons incident on the samples, were calculated according to the increasing energy, and the changes of these values depending on the energy of the neutrons are given in Figure 4. When the figure is examined, the HVL values of all HEA samples are lower than paraffin. This result shows that all HEA samples have a higher absorption capacity than paraffin. The HVL value of the HEA1 sample is lower than that of 316LN stainless steel, which means that this sample has a superior absorption ability than 316 LN stainless steel.

HEA2 and HEA3 samples also have HVL values close to 316LN, and they showed good shielding properties.
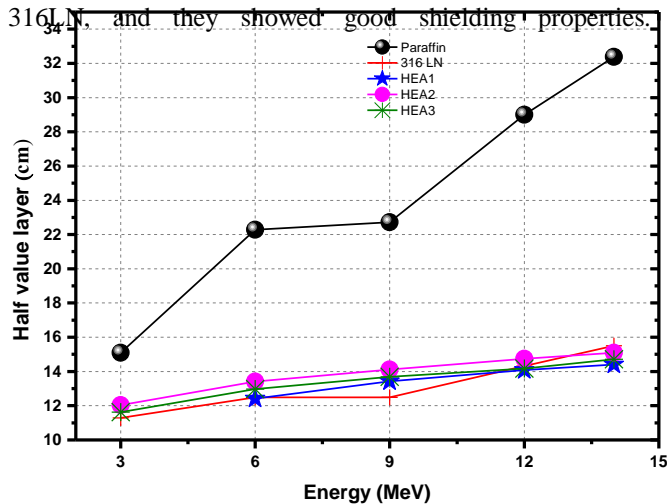
Figure 4. Change of HVL values in the energy range of 3-14 MeV

5. Conclusion

In this study, fast neutron absorption parameters of high entropy alloys with chemical content HEA1 (Ti25Ta25Hf25Nb25), HEA2 (Ti20Ta20Hf20Nb20Zr20), HEA3 (Ti20Ta20Hf20Mo20Zr20) were determined theoretically by Monte Carlo code. The shielding capacity of all examined HEA samples against neutron radiation was determined. It was observed that the neutron suppression power of all HEA samples was superior to the paraffin commonly used in shielding studies. It was determined that the neutron radiation stopping power of all examined HEA samples was higher than paraffin. In particular, the neutron radiation absorption capacity of the HEA1 sample was found to be greater than that of the reference sample, 316 LN nuclear stainless steel, and all other samples. However, it was observed that the absorption capacities of HEA2 and HEA3 samples were close to 316 LN samples. According to all results, it was determined that these HEA samples, which have excellent resistance to high temperatures as well as superior mechanical and structural properties, can be used as shielding materials to prevent neutron radiation leaks, especially in nuclear reactors, radiotherapy rooms, transportation and storage of used radioactive wastes, and it was suggested that they can be used safely in these applications.

References

AGOSTINELLI, S., ALLISON, J., AMAKO, K., APOSTOLAKIS, J., ARAUJO, H., ARCE, P., ASAI, M., AXEN, D., BANERJEE, S., BARRAND, G., BEHNER, F., BELLAGAMBA, L., BOUDREAU, J., BROGLIA, L., BRUNENGO, A., BURKHARDT, H., CHAUVIE, S., CHUMA, J., CHYTRACEK, R., COOPERMAN, G., COSMO, G., DEGTYARENKO, P., DELL'ACQUA, A., DEPAOLA, G., DIETRICH, D., ENAMI, R., FELICIELLO, A., FERGUSON, C., FESEFELDT, H., FOLGER, G., FOPPIANO, F., FORTI, A., GARELLI, S., GIANI, S., GIANNITRAPANI, R., GIBIN, D., GOMEZ CADENAS, J.J., GONZALEZ, I., GRACIA ABRIL, G., GREENIAUS, G., GREINER, W., GRICHINE, V., GROSSHEIM, A., GUATELLI, S., GUMPLINGER, P., HAMATSU, R., HASHIMOTO, K., HASUI, H., HEIKKINEN, A., HOWARD, A., IVANCHENKO, V., JOHNSON, A., JONES, F.W., KALLENBACH, J., KANAYA,

Investigation of epithermal and fast neutron shielding properties of Some High Entropy
Alloys Containing Ti, Hf, Nb, and Zr

EAJS, Vol. VIII Issue II |43

N., KAWABATA, M., KAWABATA, Y., KAWAGUTI, M., KELNER, S., KENT, P., KIMURA, A., KODAMA, T., KOKOULIN, R., KOSSOV, M., KURASHIGE, H., LAMANNA, E., LAMPEN, T., LARA, V., LEFEBURE, V., LEI, F., LIENDL, M., LOCKMAN, W., LONGO, F., MAGNI, S., MAIRE, M., MEDERNACH, E., MINAMIMOTO, K., MORA DE FREITAS, P., MORITA, Y., MURAKAMI, K., NAGAMATU, M., NARTALLO, R., NIEMINEN, P., NISHIMURA, T., OHTSUBO, K., OKAMURA, M., O'NEALE, S., OOHATA, Y., PAECH, K., PERL, J., PFEIFFER, A., PIA, M.G., RANJARD, F., RYBIN, A., SADILOV, S., DI SALVO, E., SANTIN, G., SASAKI, T., SAVVAS, N., SAWADA, Y., SCHERER, S., SEI, S., SIROTENKO, V., SMITH, D., STARKOV, N., STOECKER, H., SULKIMO, J., TAKAHATA, M., TANAKA, S., TCHERNIAEV, E., SAFAI TEHRANI, E., TROPEANO, M., TRUSCOTT, P., UNO, H., URBAN, L., URBAN, P., VERDERI, M., WALKDEN, A., WANDER, W., WEBER, H., WELLISCH, J.P., WENAUS, T., WILLIAMS, D.C., WRIGHT, D., YAMADA, T., YOSHIDA, H., ZSCHIESCHE, D. (2003). GEANT4 - A simulation toolkit. Nuclear Instruments and Methods in Physics Research, Section A: Accelerators, Spectrometers, Detectors and Associated Equipment.

AYGUN, B., ALAYLAR, B., TURHAN, K., ŞAKAR, E., KARADAYI, M., SAYYED, M.I., PELIT, E., GULLUCE, M., KARABULUT, A., TURGUT, Z., ALIM, B. (2020). Investigation of neutron and gamma radiation protective characteristics of synthesized quinoline derivatives. International journal of radiatıon biology.96 (11), 1423-1434.

ALIM, B., OZPOLAT, OF., ŞAKAR, E., HAN, I., ARSLAN, I., SINGH, VP., DEMİR, L. (2022). Precipitation-hardening stainless steels: Potential use radiation shielding materials. Radiation Physics and Chemistry. 194.110009.

AYGUN, B., (2019 a). High alloyed new stainless steel shielding material for gamma and fast neutron radiation. Nuclear Engineering and Technology. 52(3), 647-653.

AYGUN, B., KORKUT, T., KARABULUT, A., GENCEL, O. (2015). Production and Neutron Irradiation Tests on a New Epoxy/Molybdenum Composite.

International Journal of Polymer Analysis and Characterization. 20(4), 323-329.

AYGUN, B., ŞAKAR, E., CINAN, E., YORGUN, NY., SAYYED, MI., AGAR, O., KARABULUT, A. (2020 a). Development and production of metal oxide doped glasses for gamma ray and fast neutron shielding. Radiation Physics and Chemistry.174, 108897.

AYGUN, B., KARABULUT, A. (2018). Development and Production of High Heat Resistant Heavy Concrete Shielding Materials for Neutron and Gamma Radiation. Eastern Anatolian Journal of Science 4 (2), 24-30.

AYGUN, B., ŞAKAR, E., KARABULUT, A., ALIM, B., SAYYED, MI., SINGH, VP., YORGUN, NY., OZPOLAT, ÖF. (2020b). Development of SiO_2 based doped with LiF, Cr_2O_3, CoO_4 and B_2O_3 glasses for gamma and fast neutron shielding. Radiochimica Acta. 109(2), 143-151.

AYGUN, B., ŞAKAR, E., KORKUT, T., SAYYED, MI., KARABULUT, A. (2019c). New high temperature resistant heavy concretes for fast neutron and gamma radiation shielding. Radiochimica Acta. 107(4).

AYGUN, B., ŞAKAR, E., KORKUT, T., SAYYED, MI., KARABULUT, A., ZAID, MHM. (2019b). Fabrication of Ni, Cr, W reinforced new high alloyed stainless steels for radiation shielding applications. Results in Physics. 12, 1-6.

BILICI, I., AYGUN, B., DENIZ, CU., OZ, B., SAYYED, MI., KARABULUT, A. (2021). Fabrication of novel neutron shielding materials: Polypropylene composites containing colemanite, tincal and ulexite. Progress in Nuclear Energy. 141,103954.

EID, EA., SADAWY, MM., REDA, AM. (2022). Computing the dynamic friction coefficient and evaluation of radiation shielding performance for AISI 304 stainless steel. Materials Chemistry and Physics. 277, 125446.

EL-AGAWANY, FI., EKINCI, N., MAHMOUD, KA., SARITAŞ, S., AYGUN, B., AHMED, EM., RAMMAH, YS. (2021). Gamma-ray shielding capacity of different B_4C-, Re-, and Ni-based superalloys. European Physical Journal Plus. 136.527.

ELSAFI, M., EL-NAHAL, MA., SAYYED, MI., SALEH, IH., ABBAS, MI. (2021). Effect of bulk and nanoparticle Bi_2O_3 on attenuation capability of radiation shielding glass. Ceramics International. 47(14), 19651–19658.

GUREL. S., YAGCI, MB., CANADINC, D., GERSTEIN, G., BAL, B., MAIER, HJ. (2021). Fracture behavior of novel biomedical Ti-based high entropy alloys under impact loading. Materials Science and Engineering: A. 803,140456.

HU, G., SHI, G., HU, H., YANG, Q., YU, B., SUN, W. (2020). Development of gradient composite shielding material for shielding neutrons and gamma rays. Nuclear Engineering and Technology. 52(10), 2387-2393.

KAREER A, WAITE JC, LI B, COUET A, ARMSTRONG DEJ, WILKINSON AJ. (2019). Short communication: 'Low activation, refractory, high entropy alloys for nuclear applications.' Journal of Nuclear Materials. 526, 151744.

KING DJM, CHEUNG STY, HUMPHRY-BAKER SA, PARKIN C, COUET A, CORTIE MB, LUMPKIN GR, MIDDLEBURGH SC, KNOWLES AJ. (2019). High temperature, low neutron cross-section high-entropy alloys in the Nb-Ti-V-Zr system. Acta Materialia. 166, 435–446.

KING, D.; BURR, P.; OBBARD, E.; MIDDLEBURGH, S. DFT. (2017). Study of the hexagonal high-entropy alloy fission product system. J. Nucl.Mater. 488, 70–74.

KINNO M, KIMURA KI, NAKAMURA T. (2002). Raw materials for low-activation concrete neutron shields. Journal of Nuclear Science and Technology. 39(12), 1275–1280.

KORKUT T, AYGUN B, BAYRAM O, KARABULUT A. (2015). Study of neutron attenuation properties of super alloys with added rhenium. Journal of Radioanalytical and Nuclear Chemistry. 306, 119–122.

MARY SJ, NAGALAKSHMİ R, EPSHIBA R. (2015). High entropy Alloys propertıes and ıts applications-an overvıew. High entropy alloys Section B-Review Eur Chem Bull. 4(6), 279–284.

TEKIN, HUSEYIN OZAN, ALMISNED, GHADA, ZAKALY, HESHAM M. H., ZAMIL, ABDALLAH, KHOUCHEICH, DALIA, BILAL, GHAİDA, AL-SAMMARRAIE, LUBNA, ISSA, SHAMS A. M., AL-BURIAHI, MOHAMMED SULTAN AND ENE, ANTOANETA. (2022). Gamma, neutron, and heavy charged ion shielding properties of Er^{3+}-doped and Sm^{3+}-doped zinc borate glasses" Open Chemistry. 20 (1),130-145.

PICKERING EJ, CARRUTHERS AW, BARRON PJ, MIDDLEBURGH SC, ARMSTRONG DEJ, GANDY AS. (2021). High-entropy alloys for advanced nuclear applications. Entropy. 23(1), 1-28.

RAMMAH YS, MAHMOUD KA, MOHAMMED FQ, SAYYED MI, TASHLYKOV OL, EL-MALLAWANY R. (2021). Gamma ray exposure buildup factor and shielding features for some binary alloys using MCNP-5 simulation code. Nuclear Engineering and Technology. 53(8), 2661-2668.

SAHADATH, H., MOLLAH, A.S., KABIR, K.A., FAZLUL HUQ, M. (2015). Calculation of the different shielding properties of locally developed ilmenite-magnetite (I-M) concrete. Radioprotection. 50 (2), 203–207.

SARIYER D, KÜÇER R. (2020). Effect of Different Materials to Concrete as Neutron Shielding Application. Acta Physıca Polonıca A. 137, 1-4.

SCHOBER H. (2014). An introduction to the theory of nuclear neutron scattering in condensed matter. Journal of Neutron Research. 17(3), 109-357.

SINGH VP, BADIGER NM. (2014). Gamma ray and neutron shielding properties of some alloy materials. Annals of Nuclear Energy. 64, 301-310.

WANG KAIZHAO, HU J, CHEN T, ZHANG W, FAN H, FENG Y, ZHAO Z, WANG KAİJUN. (2021). Flexible Low-Melting Point Radiation Shielding Materials: Soft Elastomers with GaInSnPbBi High-Entropy Alloy Inclusions. Macromolecular Materials and Engineering. 306(12), 2100457.

WRIXON AD. (2013). Radiation. In: Safety at Work. Routledge. London 18.

YIN S, WANG H, WANG S, ZHANG J, ZHU Y. (2022). Effect of B_2O_3 on the Radiation Shielding Performance of Telluride Lead Glass System. Crystals. 178 (12), 2-10.

ZINKLE, S. Radiation-Induced Effects on Microstructure. InComprehensive Nuclear Materials; Elsevier: Amsterdam, The Netherlands, 2012; pp. 65–98

NOTLAR

NOTLAR